UNIVERSITAT POLITÈCNICA DE VALÈNCIA

UNIVERSITAT POLITÈCNICA DE VALÈNCIA

School of Industrial Engineering

Design of supported metal catalysts for ammonia cracking

Master's Thesis

Master's Degree in Chemical Engineering

AUTHOR: Krug San Martín, Javier

Tutor: Palomares Gimeno, Antonio Eduardo

Cotutor: Martínez Sánchez, Mª Cristina

External cotutor: Serna Merino, Pedro Manuel

ACADEMIC YEAR: 2024/2025

DESIGN OF SUPPORTED METAL CATALYSTS FOR AMMONIA CRACKING

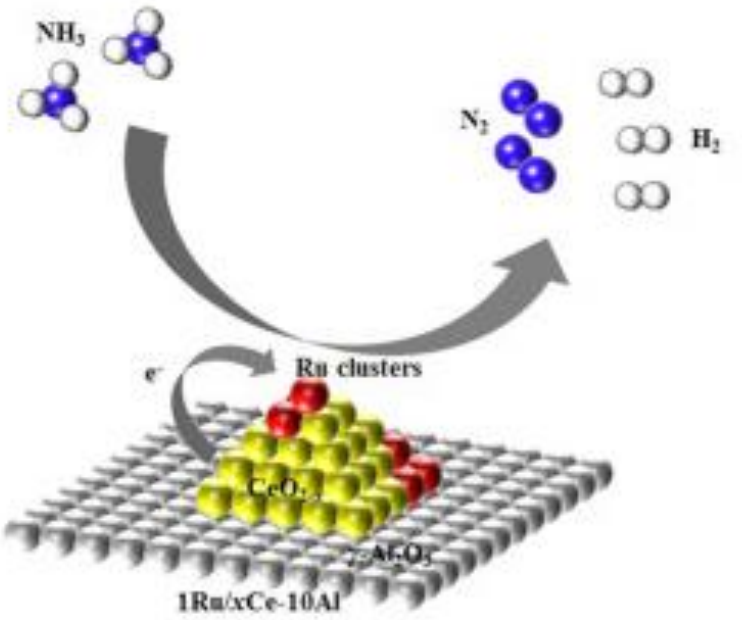

Author: Javier Krug San Martin

Codirector: María Cristina Martínez Sánchez

Codirector: Pedro Serna Merino

UPV director: Antonio Eduardo Palomares Gimeno

CONTENTS

ABSTRACT

The combustion of hydrogen releases water as the only byproduct and, thus, clean energy. Hydrogen can be obtained from different sources, but green hydrogen obtained by water electrolysis is the most preferred production route, to minimize the overall CO_2 footprint. Renewable energies, such as solar or wind, are the origin of the electricity employed in water splitting to produce green hydrogen. However, not all countries have access to renewable energies due to geographical, as well as technological reasons, something that slows down their energy transition. Despite a potentially relevant role in reducing global warming emissions, hydrogen has two main problems: storage and transport. As a result, hydrogen vectors, that is, molecules that can produce hydrogen readily, and are more easily stored and transported, have been proposed as a solution. Ammonia and methanol are two vectors that can operate at rather mild temperatures and pressure, and can benefit from existing pipelines, leading to cost reduction. In this strategy, countries with access to renewable energy produce hydrogen vectors (e.g. ammonia via the Haber-Bosch process) that are transported and sold to countries with limited or no access to renewable energy. The energy vector can be then stored and used by the receiving country, producing green H_2, in the case of ammonia, via ammonia cracking, through flexible, clean, and rather simple approach.

Ammonia cracking is Haber-Bosch reverse reaction. This reaction is an exothermic reaction with two subproducts: hydrogen and nitrogen. Ammonia cracking requires a high reaction temperature which increases hydrogen cost. Several metals have been studied such as Ruthenium, Cobalt, Iron or Niquel. Ruthenium appears to be a solution to reduce reaction temperature, compared with other active metals can reduce reaction temperature reducing operational costs but at the same time ruthenium is a very expensive metal, increasing the need of an optimal support to disperse the ruthenium correctly.

Several supports have been studied: alumina. Magnesium oxide, cerium oxide, hydrotalcite and silicon oxide. Solids have been impregnated by incipient wetness impregnation, dried and reduced with hydrogen to activate. Catalysts have been characterized by employing X-rays fluorescence, XRD and TEM. The equipment has been set up calibrating the following devices: mass flowmeters, furnace and analysis equipment. Activity and stability tests have been carried out to each solid to evaluate and compare solids.

Silicium oxide shows the highest activity and hydrogen production whereas cerium oxide, despite having an appropriate surface to anchor ruthenium particles and having acid behavior, shows lower activity. On the other hand, alumina's activity decreases in the stability test making it inappropriate for ammonia cracking. The economical perfective catalysts have similar reaction cost.

ACKNOWLEDGEMENTS

First of all, I would like to express my gratitude to all the people involved in this work. Not only people from ITQ but also my friends and my family, without their support in the toughest moments of this year this work wouldn't have been finished. Specially I would like to be thankful to Benji and Aroa that their help has been crucial in this research and always been kind to my, understanding my situation, all the best for them in their future challenges.

1.INTRODUCTION

1.1. ENVIRONMENTAL BACKGROUND

Global energy consumption has increased dramatically due to an increasing industrialization, a fast economic growth and a technological development in developed countries. According to the International Energy Agency survey, worldwide energy increased by 4.5%, or over 1000 TWh, in 2021, corresponding to an increase of 5% in the CO2 emissions. Figure 1 shows the CO2 emissions during the last 50 years.

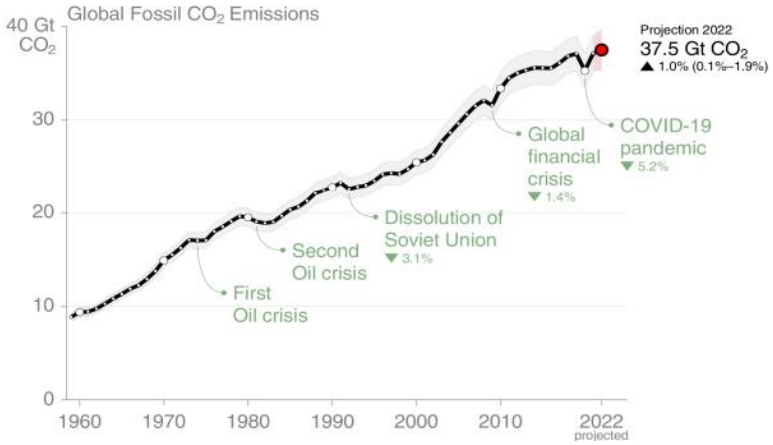

Figure 1. *Evolution of carbon dioxide emissions in the last 50 years.*(Report, 2022)

The repercussions of climate change are manifesting globally in more irregular and intense weather events, increasing sea levels, and alterations in ecosystems that lead to biodiversity harm. The primary driver of this phenomenon lies in escalating concentration of greenhouse gases such as CO_2 or methane. Carbon dioxide, a prominent greenhouse gas, contributes approximately 76% to the greenhouse effect. The intergovernmental Panel on Climate Change warns that persisting carbon dioxide accumulation could raise the global average temperature about 2 °C by 2100. (Report, 2022)

Burning fossil fuels and deforestation stand as the primary contributors to the increasing concentration of atmospheric carbon dioxide. Approximately 80% of the world's energy production, is derived from fossil fuels, thereby elevating the levels of carbon dioxide in the atmosphere. Forests, covering 30% of the land areas on Earth, serve as vital reservoirs storing between 33% - 46% of the organic carbon available on land. Their crucial role in carbon conservation and their potential to absorb carbon dioxide make them essential for mitigating the effects of the climate change.(Report, 2022)

In 2015, all the countries in the United Nations adopted the 2030 Agenda for Sustainable Development. This agenda sets out 17 Goals, which include 169 targets. These wide-ranging and ambitious goals are interconnected, as shown in Figure 2. The sustainable development goals apply to the following areas: education, health, economy, equality, justice, and environment protection. This research is focused on environment protection without harming the economy. The economy must evolve to a sustainable phase to ensure the preservation of the environment.

Renewable technologies are considered as clean energy sources and the optimal use of these resources minimizes environmental impacts, reduces the production of secondary wastes and is a sustainable alternative based on current and future economic and social needs. Sun is the source of all energies. The primary forms of the solar energy are the heat and light. Sun light and heat are transformed and

absorbed by the environment in multiple ways. Some of these transformations result in renewable energy flows such as biomass or wind energy. Renewable energy technologies provide an excellent opportunity for mitigation of greenhouse gas emissions and for the reduction of global warming by substitution of fossil fuels.

Renewable energy sources are those that can be used to produce unlimited energy based on solar, wind, biomass, geothermal-based energy, etc. Renewable energy sources that meet domestic energy requirements have the potential to provide energy services with zero or almost zero emissions of both air pollutants and greenhouse gases. In addition, their implementation will help giving a solution to the energy distribution, harvesting the renewable energy in a decentralized manner to meet rural and small-scale energy needs in a reliable, affordable and environmentally sustainable way (Panwar et al., 2011).

As it can be seen in Table 1, renewable energies will take over an important proportion of the total energy production by 2040, and the most important renewable technologies are expected to be photovoltaics and wind.

Table 1. *Evolution of renewable energy with the time*(Panwar et al., 2011).

	2001	2010	2020	2030	2040
Total consumption (million tons oil equivalent)	10,038	10,549	11,425	12,352	13,310
Biomass	1080	1313	1791	2483	3271
Large hydro	22.7	266	309	341	358
Geothermal	43.2	86	186	333	493
Small hydro	9.5	19	49	106	189
Wind	4.7	44	266	542	688
Solar thermal	4.1	15	66	244	480
Photovoltaic	0.1	2	24	221	784
Solar thermal electricity	0.1	0.4	3	16	68
Marine (tidal/wave/ocean)	0.05	0.1	0.4	3	20
Total RES	1,365.5	1,745.5	2,964.4	4289	6351
Renewable energy source contribution (%)	13.6	16.6	23.6	34.7	47.7

Despite being the most promising renewable resources, several problems must be solved such as the localizations of the wind generators and the efficiency of the photovoltaic cells. Wind farms need an average wind speed 6 -7 m/s. On the other hand, photovoltaic cells must increase electricity production efficiency, and nowadays challenge is the reduction of the surface needed for electricity production in order to reduce costs. Perovskites appear to be the solution to increase efficiency (Sun et al., 2012).

Meanwhile electrical infrastructure is developed carbon dioxide emissions have to be reduced to avoid irreversible consequences of global warming. Regarding the approaches described for reducing CO2 emission and concentration in the atmosphere, here are several technologies being developed for the capture, transport, storage, and utilization of carbon dioxide. Chemical absorption using aqueous amine solutions has been used to remove carbon dioxide from natural gas. Recent developments in polymeric membranes demonstrated to be appropriate for CO_2 removal. Polaris membrane is now available commercially and has been employed to remove carbon dioxide from syngas. In addition, polymeric membranes can be used in coal-fired thermal plants to capture the carbon dioxide in the emission focus. (Zhu et al., 2023)(Rasool et al., 2023)

The technologies for CO_2 transport are well established. There are 46500 km of CO_2 pipelines worldwide (both on-shore and off-shore), most of which are associated with enhanced oil recovery (EOR) operation in the United States. The technology for CO_2 transport with ships is also very developed and is currently being used in commercial applications. (Yang et al., 2011)

Several commercial CO2 utilization processes are mature technologies. Most are in the food and beverage industry and some in chemical production (e.g., urea, methanol). Several processes utilize

CO2 for mineral carbonation, for example, the one in the Searles Valley plant (US). In Saga City, Japan, CO2 capture from waste incineration is utilized for the cultivation of crops and algae. The CO2 for each process is mainly sourced from chemical industry units (e.g., fertilizers or ammonia production, ethylene glycol plants), but some processes capture the CO2 from power plant flue gas.(Sims et al., 1999)

In this scenario, and taking into consideration what has been exposed above, hydrogen is one of the future energetical vectors. As a fuel, it is the most benign from the environmental point of view, as its combustion produces only water, without the formation of any other subproducts. Several processes can produce hydrogen. The cleanest and most sustainable way for hydrogen production is by water splitting. The use of renewable energy sources, which is the most desirable, does not produce greenhouse gases and leads to what is known as Green Hydrogen. Wind and solar energy are the most common employed to obtain for this. However, not all countries have access to this technology due to geographical, economical or meteorological reasons, so H_2 will have to be transported from locations where it can be produced to locations where H_2 is demanded. In addition, hydrogen transport and storage also present important challenges due to its physic-chemical properties (see section 1.2 for more details). In this line, the use of hydrogen vectors is a suitable alternative to transport the hydrogen. Hydrogen vectors are simple molecules containing hydrogen in their molecular structure, like methanol or ammonia, which are liquids, or which can be liquefied at lower pressures than hydrogen, decreasing the problems related to storage and transport. A scheme of the circular economy based on the use of NH_3 as H_2 vector is shown in Figure 2. ("Glob. Hydrog. Rev. 2021," 2021)

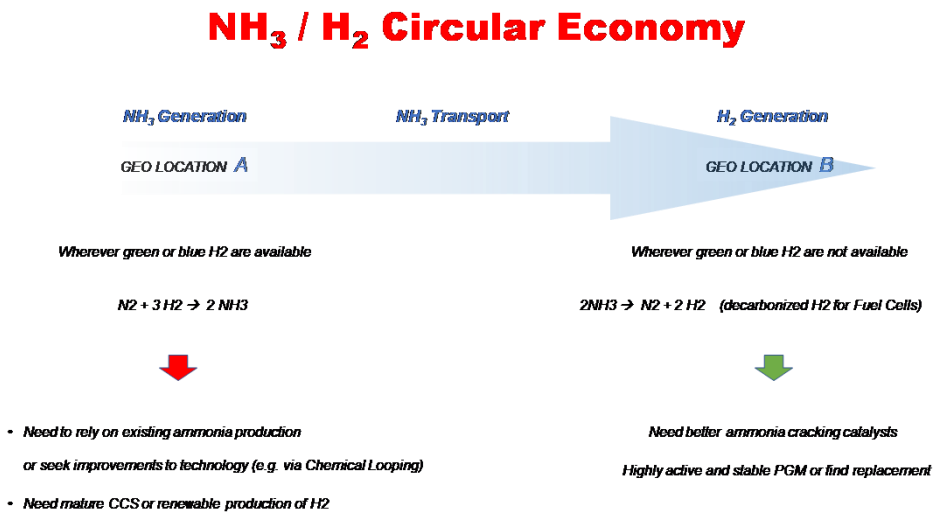

Figure 2. *Hydrogen carrier qualitative scheme.* ("Glob. Hydrog. Rev. 2021," 2021)

1.2 HYDROGEN

Hydrogen is the lightest and the most abundant chemical element in the universe. Composed by an electron and a nucleus with unique proton, it is very reactive in every physical state. Apart from standard hydrogen, known as protium, there are two main isotopes, deuterium, and tritium, with applications in various fields.

In terms of storage and transportation, hydrogen can be stored in gaseous, liquid, or solid form. For storage in gaseous form, high-pressure containers or cryogenic compression at extremely low

temperatures are most commonly used. In liquid form, significant refrigeration is required to maintain it at cryogenic temperatures, around -253 °C. It can also be stored in solid form through adsorption onto porous materials or absorption into metals. The diffusion coefficient of hydrogen is $61.17*10^6$ m^2/s, very high and responsible for causing problems in hydrogen storage. Hydrogen diffuses thought the metal producing metal hydrides and increasing the corrosion of the storage vessels. (Ball and Wietschel, 2009)

Hydrogen is classified by colours according to its origin as can be seen in Figure 3. Grey hydrogen is produced by methane steam reforming, a process that the 75% of the feed turns into hydrogen and 15% to methanol and the rest in alternative fuels. (García et al., 2010)

Brown hydrogen is generated via coal gasification, with carbon monoxide and carbon dioxide as by-products. Grey and Brown hydrogen generate significant amounts of CO_2 emissions, which is a big disadvantage. However, if the release of this CO2 is avoided by means of capture systems combined, for instance, with the methane reforming technology, the hydrogen is considered as blue. On the other hand, green hydrogen is produced by water electrolysis using renewable energy, and turquoise

Figure 3. *Hydrogen classification by origin.*

hydrogen is obtained by methane pyrolysis, leading to solid carbon as the main by-product. (Zainal et al., 2024)

Green hydrogen is a carbon neutral fuel, produced by electrolysis. The origin of the electricity is renewable, produced by several technologies based on wind, sun or geothermal energy sources. Although renewables are becoming a cheaper source of electricity around the world with increasing potential to reduce operating costs, electrolysis is still an expensive technology nowadays due to cost of the electrolysers, which present significant scale-up problems such us mass transfer limitations or electricity distribution problems.(Zainal et al., 2024)

Water splitting is an electrochemical reaction that turns water into hydrogen and oxygen using electricity. At the cathode, the water is reduced by electrons to hydrogen and negatively charged hydroxide ions. At the anode, hydroxide ions are oxidized to oxygen and water while releasing electrons. Water molecules turn into hydrogen and oxygen in the ratio of 2:1. The water splitting reaction mechanism is expressed in Equations 1,2,3:

$$\text{Cathode: } 2H_2O_{(l)} + 2e^- \rightarrow 2H_{2(g)} + 2OH^-_{(aq)} \quad (1)$$

$$\text{Anode: } 2OH^-_{(aq)} \rightarrow 0.5O_{2(g)} + H_2O_{(l)} + 2e^- \quad (2)$$

$$\text{Overall reaction: } H_2O_{(l)} \rightarrow H_{2(g)} + 0.5O_{2(g)} \quad (3)$$

The free reaction enthalpy for water electrolysis is $\Delta_R G$ = 237 kj/mol which leads to a reversible cell voltage of -1.23 V, determined by Equation 4:

$$U_{rev} = \frac{\Delta_R G}{z*F} \quad (4)$$

The reversible cell voltage is the minimum energy that the process requires without considering the resistance of the medium. The real energy supplied to the system is the sum of the following parameters: reversible cell voltage, the resistance of the medium, and the electrical resistance of the electrolysers. The resistance of the medium is determined by two factors: the temperature, and the conductivity of the medium, which depends on the concentration of cations such as sodium or potassium. (Brauns and Turek, 2020)

The electrolyser is composed by the following elements: electrolysis stack, pumps, heat exchangers, two gas separators and gas purification equipment. Pumps feed the water to the electrolysis stack. Hydrogen and water leave the stack to be separated in the gas separator in which the hydrogen and the oxygen will be fed to a purification demister/dryer to remove the impurities. Water from the gas separation step is recirculated to the electrolysis stack. Heat exchangers ensure that water enters the stack at the optimal temperature. The overall process explained above in show in Figure 4. (Brauns and Turek, 2020)

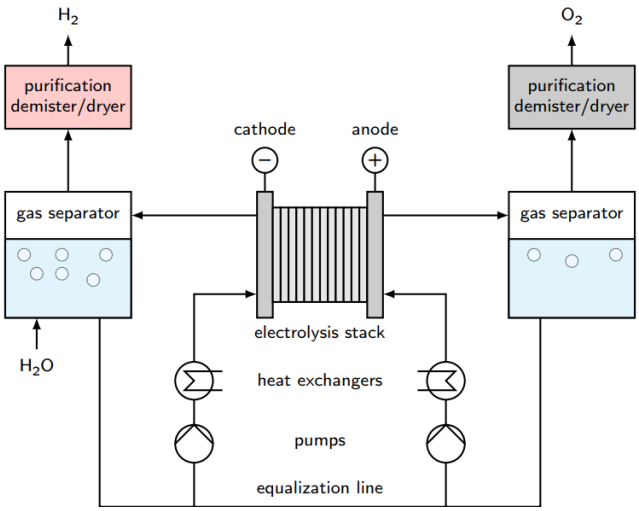

Figure 4. *Electrolyser scheme.* (Brauns and Turek, 2020)

1.2.1 HYDROGEN PROBLEMS

1.2.1.1 STORAGE

Hydrogen storage is one of the most critical factors. Without an effective storage infrastructure, a hydrogen economy will be difficult to achieve. Automotive industry is working on on-board storage of hydrogen as the most critical factor concerning hydrogen propelled vehicles. Although the physical limits for the storage density of compressed and liquid hydrogen have been reached, there is still potential in development of solid materials for hydrogen storage for this application, such as systems involving metal hydrides.(Ball and Wietschel, 2009) In metal hydrides, the hydrogen molecules split into atoms on the surface of the metal, which enter the metallic lattice diffusing through the metal, jumping between interstitial sites, and finally forming a hydride phase with a pseudo-ordered hydrogen sub-lattice. Palladium is one of the most studied metals, but due to its high cost, lanthanum nickel

hydride has been studied during the last year. However, at present, metal hydrides have not been implemented at industrial scale.

1.2.2.1 TRANSPORT

Not all the countries are able to produce green hydrogen. Besides hydrogen storage in vehicles, hydrogen transport between countries is a highly critical factor. Many approaches have been proposed to use natural gas pipelines to transport hydrogen, but pipelines' corrosion is an important drawback. Thus, the use of hydrogen vectors has been suggested to deal with these corrosion problems. Hydrogen vectors are specific molecules that may store H_2 by suffering reversible hydrogenation-dehydrogenation reactions, which lead to high storage capacity. These molecules, usually in liquid phase at ambient temperature or easier to liquefy than H_2, can be transported using existing infrastructure, ensuring safety, economical optimization, and convenience. This technology is considered a promising alternative to H_2 liquefaction or high-pressure storage and is expected to play a significant role in future hydrogen energy storage and transport. Hydrogen vectors might be classified in two groups: hydrogen-lean organic liquids that achieve fully reversible hydrogenation and dehydrogenation storage cycles, such as aromatic hydrocarbons and hydrogen-lean inorganic small molecules such as methanol or ammonia, formed by hydrogenation of carbon dioxide or nitrogen.

1.3 AMMONIA HYDROGEN CARRIER

Ammonia is a colourless gas with a chemical formula NH_3, formed by hydrogen and nitrogen. In its aqueous form, it is called ammonium hydroxide. It has a pungent smell and in its concentrated form is dangerous and caustic. It is widely used as a fertilizer. It is also used in the manufacturing of explosives such as nitrocellulose and TNT. Ammonia has lower density than the air and its molar mass is 17.031 g/mol.

As previously explained, hydrogen transport and storage are the main problem of the hydrogen industry. Ammonia has 17.8 % of hydrogen in mass, and releases nitrogen as the only by-product upon cracking. Many countries are not able to produce green hydrogen due to the scarce renewable energy resources, whereas other countries have high green hydrogen production potential. Despite of its corrosive nature, ammonia is an adequate option to be a hydrogen carrier to transport hydrogen between countries due to the facilities of storage and transport.

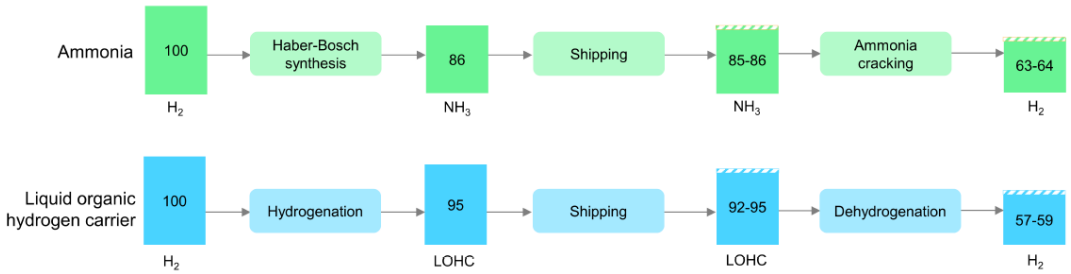

Figure 5. *Hydrogen carrier performance block diagram.*(Report, 2022)

1.3.1 GREEN AMMONIA PRODUCTION

Ammonia is produced by the Haber-Bosch process. The process consists in the direct reaction of nitrogen and hydrogen. The main difference between green ammonia and conventional ammonia is the origin of the hydrogen. Green hydrogen production has been explained above and nitrogen is obtained from Linde process distilling air. The main reaction for ammonia production is the following:

$$N_2(g) + 3H_2(g) \leftrightarrow 2NH_3(g) \;\; \Delta H^0 = -92.29\ kJ$$

Ammonia production is a reversible exothermic reaction. As it involves a reduction in the number of mols, and all components are in gas phase, the reaction is favoured at high pressures based on Le Chatelier's principle. On the other hand, despite of being an exothermic reaction, working temperatures are high due to kinetic limitations. Moreover, the Haber-Bosch process relies on catalyst to accelerate nitrogen hydrogenation.

The catalyst employed in the industrial process are solid, commonly iron oxide promoted with potassium oxide or aluminium oxide to improve activity.

1.3.2 AMMONIA STORAGE AND TRANSPORT

The containers used to store ammonia range from tiny containers to huge tanks. These containers can be either cylindrical or spherical, in function of storage capacity and safety requirements. Materials such as high-strength or fine-grained steels are used, but they can be susceptible to stress corrosion cracking from ammonia. Water control is a key parameter to reduce material corrosion in these cases. Furthermore, temperature control is crucial to store ammonia, as it must be kept at -33 °C and at low pressures. Ammonia is stored by the following technologies:

- Atmospheric storage at -33 °C in insulated cylindrical tanks for around 50,000 tons per tank.
- Pressure storage at ambient temperature in spherical or cylindrical pressure vessels with capacities up to 1,500 tons per vessel.
- Semi-refrigerated storage at 0 °C in insulated, usually spherical pressure vessels for quantities up to about 2,500 tons.

Liquid ammonia is transported in tankers, ships, barges, by pipelines, by railcars and by trucks. Most of the times ammonia is transported in liquid state, but it must be liquefied by pressure or temperature. Transporting ammonia by pipelines is the most efficient method. However, in these cases it must be pressurized up to 20 bar to prevent gas formation and heated at least to 2°C to avoid brittle fracture in the pipeline, which in most cases means that it must be warmed at the supply terminal and cooled again to -33 °C at the receiver terminal. Additionally, ammonia requires pipeline infrastructure has to be developed to carry future ammonia demand.("AMMONIA TRANSPORT &," n.d.)

1.3.3 AMMONIA CRACKING

Ammonia cracking is the decomposition of ammonia to obtain hydrogen and nitrogen. It is a reversible endothermic reaction that will be favoured at low pressures and high temperatures.

$$2NH_3(g) \leftrightarrow N_2(g) + 3H_2(g) \quad \Delta H^0 = 46.22\ kJ/mol$$

Ammonia decomposition reaction is a gas-phase reaction employing a solid catalyst and a packed-bed reactor. In order to reduce equipment corrosion, the feed is usually diluted. For ruthenium-supported catalysts, described in the literature, the mechanism followed is the one described by Equations 5, 6, 7, 8, 9 and 10. First, there is a molecular adsorption of ammonia to give surface adsorbed ammonia at the active sites of metal catalysts. Then via successive dehydrogenation of the adsorbed ammonia, there is the formation of adsorbed nitrogen and hydrogen atoms. Finally, through recombinative desorption of nitrogen and hydrogen, there is a release of molecular nitrogen and hydrogen into the gas phase.

$$NH_3 + * \rightarrow NH_3 * \tag{5}$$

$$NH_3 * + * \rightarrow NH_2 * + H * \tag{6}$$

$$NH_2 * + * \rightarrow NH * + H * \quad (7)$$

$$NH * + * \rightarrow N * + H * \quad (8)$$

$$N * + N * \rightarrow N_2 \quad (9)$$

$$H * + H * \rightarrow H_2 \quad (10)$$

Although the mechanism of ammonia decomposition is still unclear, it is widely accepted that the cleavage of N−H bond and the recombination of surface N atoms for N2 desorption are rate-determining steps. The “electron donating effect” of Ru-based catalysts promotes electron transfer and accelerates the rate-limiting steps.(Spatolisano et al., 2023)

Several metals have been studied to analyse the effect on this reaction such us Ruthenium, Niquel, Cobalt or Iron. Magnesium oxide, Silica or Cerium oxide are some of the several supports employed to produce catalysts for ammonia cracking. However, industrially accepted minimum conversions are reached at very high temperatures which increases reaction cost. Ruthenium shows more possibilities to reduce reaction temperature optimizing the supports features, metal clusters size and the total quantity of metal in the support.

Ru particles are active for NH3 decomposition. Ru-based catalysts have high activity induced by active B5-type surface sites. According to recent studies, optimal number of B5-type sites could be obtained when the Ruthenium particle size between 3 and 6 nm.

During ammonia decomposition, the excessive presence of adsorbed nitrogen on the surface inhibits further contact between ammonia molecules and active sites, leading to catalyst deactivation. In Figure 6, can be appreciated the energy diagram between RU-N interaction, estimating the activation energy for ammonia desorption.

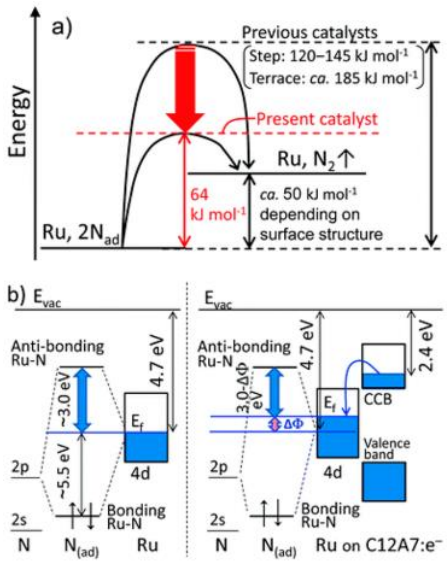

Figure 6. *Ruthenium-nitrogen interaction scheme.*(Chen et al., 2021)

Metal-based catalysts are usually supported on a solid, aiming to increase the available metallic surface area, to stabilize the active species and to increase mechanical stability. Moreover, the chemical nature of the support can also influence the final catalytic performance due to its interaction with the metal dispersed on its surface.

Alumina is very commonly employed as a support due to its high specific surface area, which enables the stabilization of small particles of metals, metal oxides and metal sulphides, and even as a catalyst because of its acid-base properties.(Brito et al., 2019)

Magnesium oxide has basic nature, basic sites that will positively enhance the metal-support interaction via electron donation, thus affecting the geometric and electronic properties of supported Ruthenium particles and, consequently, enhancing the catalytic activity of Ru-based catalysts for ammonia decomposition. (Fang et al., 2023)

Silicon dioxide (SiO_2) has been described as an excellent support for different catalysts (Lee and Park, 2022), also when combined with ruthenium (Ru) for processes like ammonia cracking. Ruthenium, known for its high catalytic activity in hydrogen-related reactions, benefits significantly from SiO_2 as a support, as the SiO_2 structure stabilizes and disperses ruthenium particles, increasing the active surface area and preventing sintering at high temperatures. In ammonia cracking, this Ru/SiO_2 system enhances the production of hydrogen by breaking down NH_3 into nitrogen and hydrogen efficiently.

Cerium oxides (CeO_2) are highly effective in catalysis due to their redox properties and oxygen storage capacity (OSC), making them excellent supports for metals like ruthenium (Ru). The Ce^{4+}/Ce^{3+} redox cycle facilitates oxygen transfer, which enhances the catalytic activity of ruthenium in reactions like CO oxidation, water-gas shift, and hydrogenation processes. Ruthenium, when supported on cerium oxides, benefits from the high oxygen mobility and surface area of CeO_2, improving its dispersion and reactivity. This synergy between cerium oxides and ruthenium makes them a powerful combination for efficient catalysis in energy and environmental applications.

Hydrotalcites belong to a class of anionic clay minerals also known as layered double hydroxides. They have divalent and trivalent cations and an intercalated anion. Structurally, they are formed by brucite-like magnesium hydroxide sheets where isomorphous substitution of magnesium cation by trivalent cation like aluminium ion occurs. The positive charge of the layer is compensated by anions, which occupy the interlayer space along with water molecules.(Climent et al., 2004)

From the catalytic perspective, hydrotalcites own unique properties such as, anion exchange capacity, high surface area and tuneable acid-base properties, which provides these materials with an amphoteric behaviour and with the capacity of giving or taking electrons from the medium accordingly (Wattanakit et al., n.d.)

In Table 2 are shown the acid/base behaviour of each support studied and the value of the surface area. Parameters that will be required to discuss the results obtained in the reaction. High surface area and basic behaviour are suitable features for highly active performance.

***Table 2**. Supports special features.*

Support	Surface area (m^2/g)	Acidity
SiO_2	213.19	Neutral
MgO	96.53	Base
CeO_2	72.33	Acid
γ-Al_2O_4	219.34	Acid
$Mg_6Al_{12}(OH)_{16}CO_3H_2O$	257.49	Amphoterus

1.4 SUSTAINABLE DEVELOPMENT GOALS

The Sustainable Development Goals (SDGs), adopted by the United Nations in 2015, are a set of 17 interconnected goals shown in Figure 7, and designed to address global challenges and achieve a better, more sustainable future by 2030. The SDGs are ambitious and universal, applying to all countries developed and developing. They aim to end poverty and hunger, ensure good health and well-being, provide quality education, achieve gender equality, and ensure access to clean water and sanitation. Moreover, they seek to promote affordable and clean energy, decent work and economic growth, innovation and infrastructure, and reduced inequalities. Environmental sustainability is a key area, with goals dedicated to sustainable cities and communities, responsible consumption and production, climate action, life below water, and life on land. In addition, they focus on necessity of peace and justice.

Figure 7. *Sustainable development goals scheme.*

This work is focused on the environmental goals, due to the implications in the following areas: energy and responsible production and consumption. Goals 7, 9, 11, 12 and 13 are related to this research. Obtaining suitable catalysts for producing hydrogen by ammonia cracking will contribute to a faster implantation of the hydrogen industry, reducing the effects of the global warming and promoting a responsible management of the resources to help in the transformation of the economy to an environmental respectfully economy.

2. OBJECTIVES

- Synthesis, characterisation and catalytic behaviour of metal catalysts for ammonia cracking
- Specific objectives:
    - Synthesis of Ruthenium nanoparticles supported on metal oxides by incipient wetness impregnation.
    - Effect of the support on ammonia cracking: SiO_2, Al_2O_3, MgO, $Mg_6Al_{12}(OH)_{16}CO_3H_2O$ and CeO_2.
    - Characterisation of the active centres by Transmission electron microscopy, X rays diffraction and X rays fluorescence
    - Catalytic test:
        - Equipment set up:
            - Mass flowmeter calibration.
            - Furnace calibration.
            - Diameter of catalysts estimation.
            - Gas chromatography system set up.
        - Reaction:
            - Light-off curves with fresh materials, for Activity evaluation.
            - Light-off curves with materials after first use, Stability evaluation.
                - Characterization post reaction employing Transmission electron microscopy and X rays diffraction.
    - Structure/correlation: obtain a relationship between the activity of the catalysts and the support nature.
- Perform an economic analysis of ammonia cracking catalysts
    - Elaborate a budget for each reaction

3.MATERIALS AND METHODS

3.1. CATALYST SYNTHESIS

A catalyst is a substance that changes the activation energy of a reaction. Catalysts are classified by phase in two groups: Homogeneous and heterogeneous. Heterogeneous catalysis is the one employed in this research in which catalyst and reactants are in different phases. Moreover, they can be classified by their electron exchanging behaviour as acid, neutral or base, and can also incorporate redox functionalities (i.e. metals). The work for this project focused, more particularly, on the use of supported Ru nanoparticles.

The catalyst synthesis process we adopted is explained next. Typically, a metal precursor is dissolved and impregnated on the support drop by drop, after which it is dried to remove the solvent and the humidity. Then the solid is calcined to decompose the metal precursors and/or directly reduced with hydrogen to activate the metal clusters.

Dry or incipient wetness impregnation is based on limiting the solution amount to just fill the pore volume of the support. This technique avoids filtration needed for elimination of liquid excess but requires a calcination step to remove all the undesirable ions from the metal precursor and to form the metal oxides on the surface of the support. Before calcining the solid, a drying process must be carried out to eliminate the solvent for better manipulation of the solid.

The calcination temperature depends on the metal precursor employed. Calcination temperature is often determined by performing a thermogravimetric test to the metal precursor by which the mass loss is measured when the temperature increases up to certain temperature. The temperature at which the mass stops dropping is close to the minimum temperature required to eliminate all volatile ligands. For this research, calcination conditions have been obtained by making bibliographical research. (Lee and Park, 2022)

Calcination is performed in a reactor at 300 °C. Operational conditions are 1 hour at 300 °C with 100 ml/min of air and with 10 °C/min of ramp. After calcination, metal clusters are in an oxidated state. Solids are reduced with hydrogen to activate the metal clusters, producing water as a by-product. Typically, the reduction temperature is selected to match that of the reaction (600°C, maximum, in our case), to minimize the probability of additional changes in the size and geometry of the metal nanoparticles during the process. Hydrogenation operational conditions are 1 hour at 600 °C with 100 mL/min of hydrogen and with a temperature ramp of 10 °C/min.

3.2. CATALYST CHARACTERIZATION

In this section, the characterization of the synthetized catalysts is explained. Three parameters have been analysed: composition and size of Ruthenium particles. Three different characterization techniques were employed: X-ray fluorescence, X-ray diffraction (XRD) and transmission electron microscopy (STEM).

3.2.1 X RAYS FLUORESCENCE

This technique has been employed as a substitution of ICP-OES, because sample desegregation by acid treatment is difficult is some of the cases investigated, increasing the experimental error. Those samples were measured with fluorescence are easier and faster to measure.

This technique is based on the radiation that is emitted when an electron from the outermost layer of the atom moves into a vacancy in the atoms of the outermost layer of the atom moves into a vacancy

in the closest layer to the nucleus of the atom. More specifically, when an atom is irradiated with X-rays, lower-energy electrons in its innermost, lower-energy shell are ejected, generating a vacancy that will be occupied by an electron in a higher-energy outer shell and the vacancy in a higher energy outermost shell will occupy. During this dissipation of excess energy takes place in the form of photons, generating secondary X-rays that can be generating secondary X-rays that can be measured.

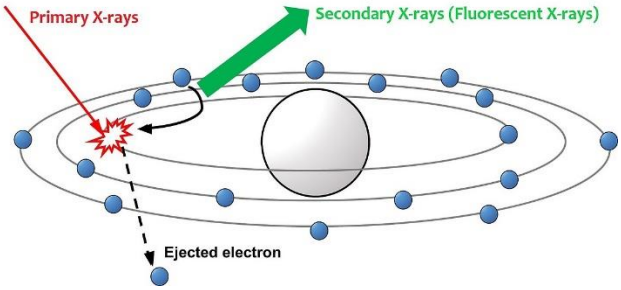

Figure 8. *X-rays fluorescence theoretical background.*

This radiation is characteristic of each element and its intensity is proportional to the amount of substance in the sample, allowing its identification and quantification. XRF measurements have been carried out without any pretreatment. For the samples studied in Chapters 4 and 5, the calibration line was obtained from standards prepared in the laboratory from mixtures of SiO_2, MgO, Al_2O_3, CeO_2 and $Mg_6Al_{12}(OH)_{16}CO_3H_2O$. Preparing mixtures of Ruthenium Nitrosyl Nitrate in different proportions to obtain a percentage by weight of ruthenium in SiO_2, MgO, Al_2O_3, CeO_2 and $Mg_6Al_{12}(OH)_{16}CO_3H_2O$ matrix of 1,2,3,4.

3.2.2 X RAYS DIFFRACTION

X-ray powder diffraction is a rapid analytical technique commonly used for phase identification of a crystalline material and provides information on unit cell dimensions. It is a non-destructive technique based on the interaction of the material with the electromagnetic field. Identification of phases is often achieved by comparing the XRD patterns of unknown sample with reference database.

When X-rays penetrate a material, they become attenuated (μ), scattered (σ), absorbed (τ) and undergo the so-called ´pair building´ (π). These parameters act additively. The transmitted intensity I depends on the incident intensity (I_0), the attenuation coefficient (μ/ρ) and the path length through the material d, as it can be shown in the Equation 12.(Diffraction, n.d.)

$$I = I_0 e^{-\mu d} \tag{11}$$

The attenuation of the sample is calculated by the Equation 13, which is the following expression.

$$\mu \sim \rho p Z^3 \lambda^3 \tag{12}$$

The runs of XRD tests are carried out in a diffractometer. This device varies the incident angle and measures the intensity to build a diffractogram. Depending on the device's geometry and the type of sample, the angle between the incident beam and the sample is fixed or variable. A general scheme of a XRD test is shown in Figure 9.

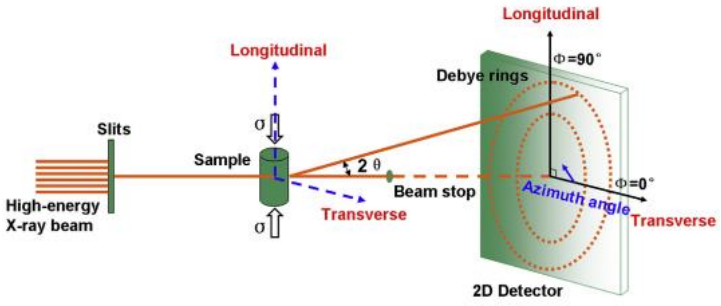

Figure 9. *XRD test scheme.*(Zhang et al., 2017)

The mathematical expression that is employed to relate the angle and the intensity of the incident beam is the Equation 14.

$$n * \lambda = 2 * d * \sin(\theta) \tag{13}$$

As it has been explained, a diffractogram must be analysed taking as a reference a diffractogram of know composition sample. In this case to examinate the existence of big Ruthenium particles the support will be taken as references and the intensity of the peaks will be examinate in the 42 degrees, where ruthenium appears.

3.2.3 STEM

This technique is based on the interactions of electrons with matter. Due to the interactions, several signals will be generated that can give information about composition, morphology, structure, and imperfections.

Electronic microscopes achieve higher resolution than optical microscopes. Electronic microscopes take atomic images due to the flux of electrons that are generated which have smaller wavelength that the photons of the visible spectra.

The interaction of accelerated electrons with the analysed surface generated the following reactions: Auger electrons, transmitted electrons, secondary electrons, retro scattered electrons, etc. The reactions are classified in elastic interactions which electrons energy is transferred to the sample and the inelastic interactions which only part of the energy is transferred to the sample (Auger electrons, transmitted electrons, secondary electrons, retro scattered electrons, etc.). The previous classification of the interactions of the electrons with the sample is shown in the Figure 10.

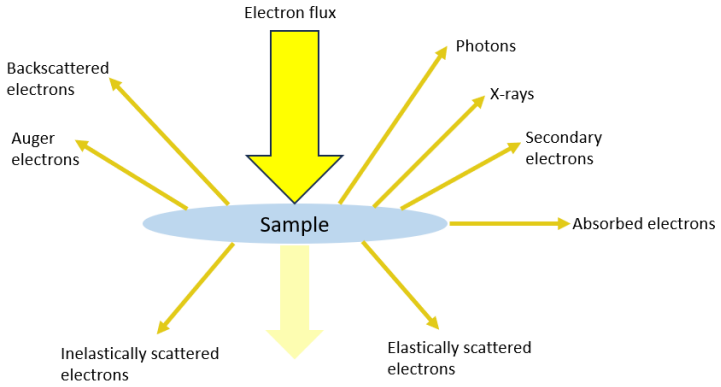

Figure 10. *TEM theoretical background.*

For this work, two different types of electronic microscope have been employed: STEM (Transmission electron microscope) and SEM (Scanning electron microscope).

The main aim of the STEM has been to analyse the size of Ruthenium nanoparticles. The images may be obtained by two different forms: analysing the transmitted electrons or analysing the dispersed electrons. The form of analysing depends on the studied elements. Scanning transmission electron microscopy (STEM) imaging of the catalysts and Energy Dispersive X-ray (EDX) studies were carried out using a JEOL electron microscope Model 2100F with an operating voltage of 200 kV.

The EDX microanalysis is a technique of elemental analysis associated to electron microscopy based on the generation of characteristic X-rays that reveals the presence of elements present in the specimens. As a result of the interaction of the electron flux with the sample, X-rays are emitted due to the difference between two orbitals involved in the transition which is thus characteristic of the element. The X-rays are analysed and turned into electric pulse in form of binding energy. The pulses are directly proportional to the quantity of the element content in the sample.(Moussa Martí, 2020)

3.3. CATALYTIC TEST

In this section, the equipment, equipment calibration, equations employed for parameter calculus and the experimental methodology are explained. The catalytic test measures the catalyst activity and stability that is evaluated by two parameters: ammonia conversion and hydrogen yield.

3.3.1 EQUIPMENT

The equipment employed in the experiments consists of a fix bed reactor, gas chromatograph Varian 3800, 6 mass flow meters, three ways valve, 4 manometers and an additional argon high pressure purge line. Equipment's flow diagram is shown in Figure 11.

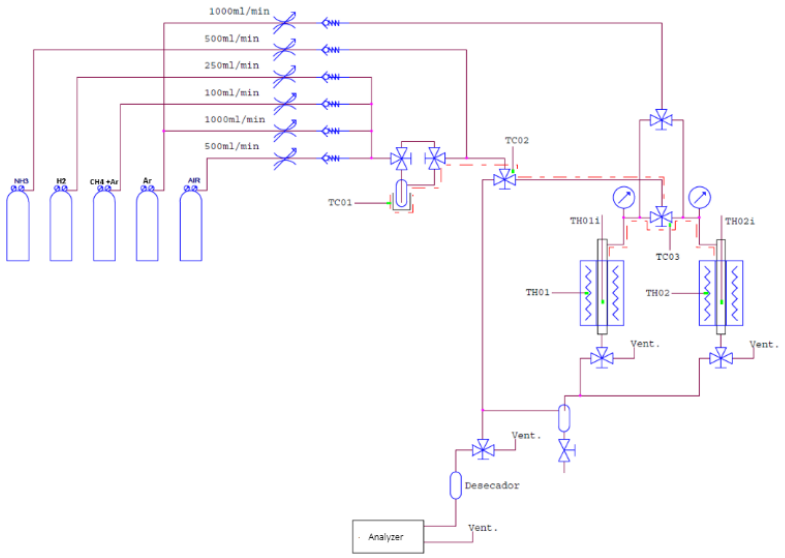

Figure 11. *Equipment flow diagram.*

Stainnless steel is the material used in the pipelines of the equipment. There are several reasons which are mentioned below for choosing stainless steel:

- High corrosion resistance
- High temperature resistance

- Easy formability and fabrication
- Low maintenance
- Very durable

Ethylene Propylene Diene Monomer (EPDM) is the material chosen to adjust the internal mechanical seals in the pipeline of the ammonia, which deteriorates the Viton rings due to the low resistance to ammonia corrosion. EPDM rubber belongs to the elastomers group. The elasticity depends on the degree of crosslinking. Ethylene-propylene-diene rubber is formed by the copolymerization of ethylene, propylene and a diene with non-conjugated double bonds with the aid of Ziegler-Natta or metallocene catalysts. Ethylene-propylene-diene rubber is non-melting and does not deform, even under the influence of heat. High temperatures cause the material to break down or decompose. EPDM is non-soluble and cannot be welded.

For pressure regulation, each gas bottle had a hand reductor to regulate the outlet gas pressure. Additionally, 2 more manometers were set up to measure the reactors pressure and chromatograph inlet pressure. Finally, to regulate chromatograph inlet pressure two devices were set up: a splitter and a needle valve.

The reactor is a tubular reactor of quartz that can perform in temperatures up to 800 °C. The geometrical scheme of the reactor is shown in Figure 12.

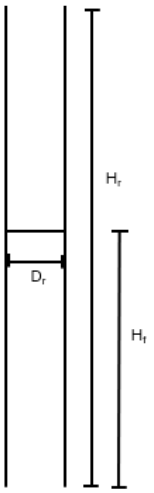

Figure 12. *Reactors geometrical scheme.*

The parameters shown in Figure 12 are reactors diameter, base height and reactors total height. The magnitudes of the parameters explained in Figure 12 are expressed in Table 3.

Table 3. *Reactors geometrical parameters.*

Parameter	Magnitude
H_r (cm)	27
D_r (cm)	1
H_f (cm)	10

The reactor is covered by a furnace to adjust reaction temperature. The furnace has 500 W of power. It is regulated by the panel shown in Figure 13 to regulate set point, temperature range and timer.

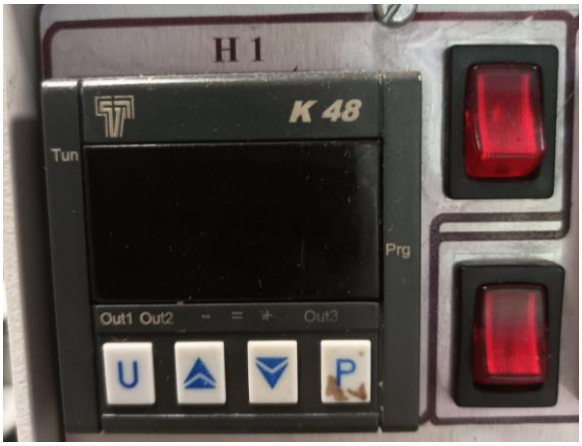

Figure 13. *Furnace control panel.*

Components of the samples are separated by a gas chromatograph. The phase inside the column retains the components depending on the chemical affinity. Chromatography columns are classified as a function of the substances that need to be separated:

For ammonia decomposition, J&W CP-Molsieve 5Å column has been chosen and the features of the column are shown in Table 4.

Table 4. *Chromatographical column features.*

Feature	Magnitude
Capillary tubing	Fused Silica
Film thickness (µm)	10
Format (inch)	7
GC Column Type	PLOT
Inner Diameter (mm)	0.32
Length (m)	30
Phase	CP-Molesieve 5 A
Temperature range (°C)	-200 /350

The analyser is a SHIMADZU BID-2010 Plus, a barrier discharge ionization detector. The barrier discharge ionization detector is constructed of two main sections, the plasma generation section and the collector section. The plasma generation section contains three electrodes and generates non-equilibrium plasma from the electrical discharge of the dielectric barrier by applying high voltage to the central electrode. Non -equilibrium plasma ionizes the sample using the photon energy emitted is accumulated and amplified and output as a voltage value.

The operational conditions stablished for a correct separation of the ammonia from methane and argon are shown in Table 5. The operational conditions are crucial to avoid incorrect separations such as methane and argon appear under the same peak.

Table 5. *chromatographical collum's operational conditions.*

Conditions	Magnitude
Temperature (°C)	150
Pressure (kPa)	108.5
Total flow (mL/min)	60.8
Colum flow (mL/min)	2.75
Linear velocity (cm/s)	42
Purge flow (mL/min)	3
Split	20

3.3.2 EQUIPMENT CALIBRATION

Equipment calibration comprises two operations: reactor calibration and analyser calibration. Bed height was determined by mapping the reactor temperature to ensure isothermal conditions, whereas particle diameter was determined to avoid mass transfer limitations according to fixed bed mass correlations. Mass flow operation range will be determined by the calibration of the mass flowmeters which belong to reactor calibration. On the other hand, the gas chromatograph section describes how the response of the analyser was quantified employing as methane as an internal standard.

3.3.2.1 FLOW METER CALIBRATION

Mass flowmeters calibration was performed employing a bubble mass flow meter. For each flow three runs were performed and the average taken. For low mass flows 10 mL of volume were taken as reference whereas for high mass flows 20 mL were taken. The calibration was performed at ambient temperature, and the results are shown in Figures 14,15,16,17,18 and 19.

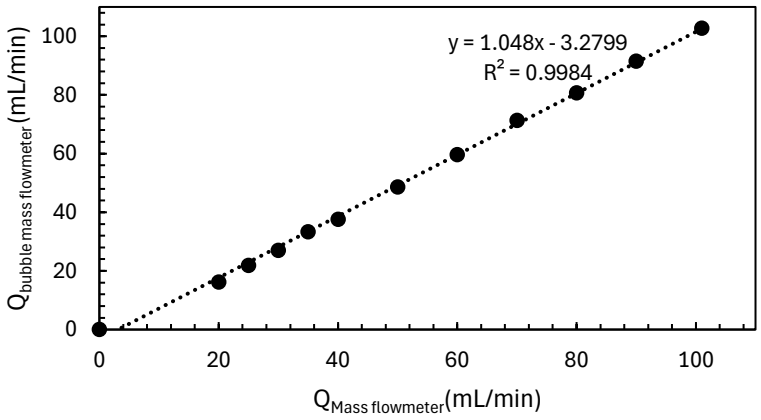

Figure 14. *Air mass flow meter calibration curve.*

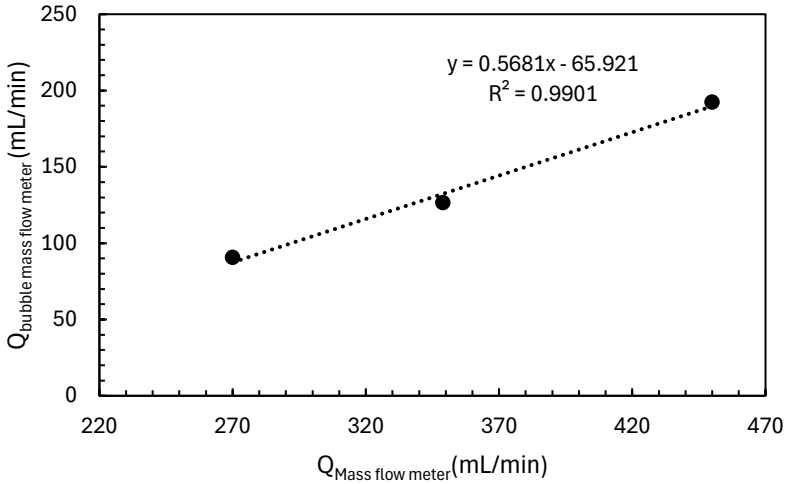

Figure 15. *Ammonia mass flow meter calibration curve.*

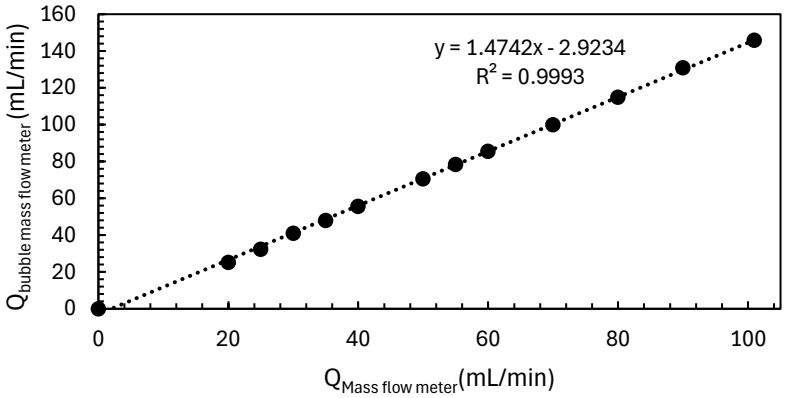

Figure 16. *Argon mass flow meter calibration curve.*

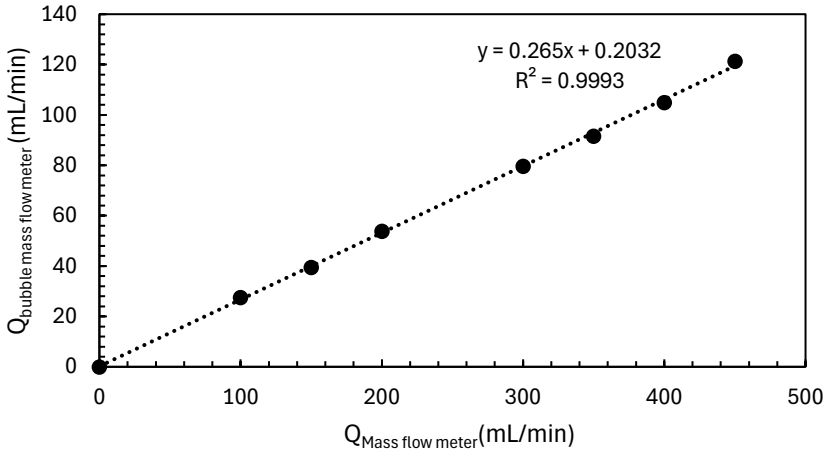

Figure 17. *Hydrogen mass flow meter calibration curve.*

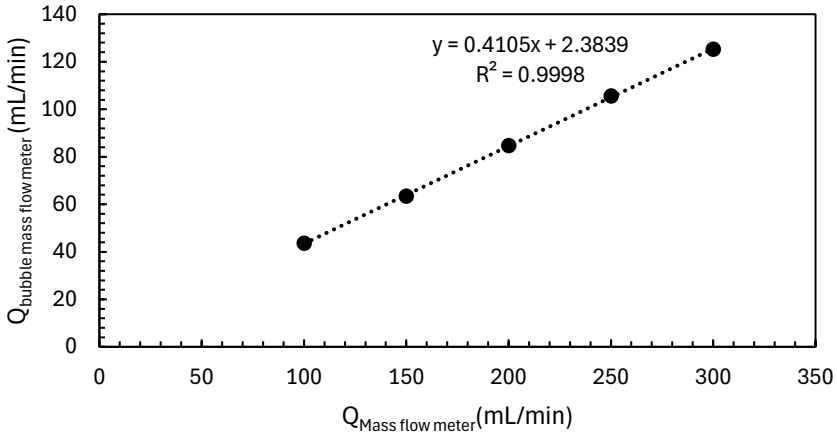

Figure 18. *Internal Standard mass flow meter calibration curve.*

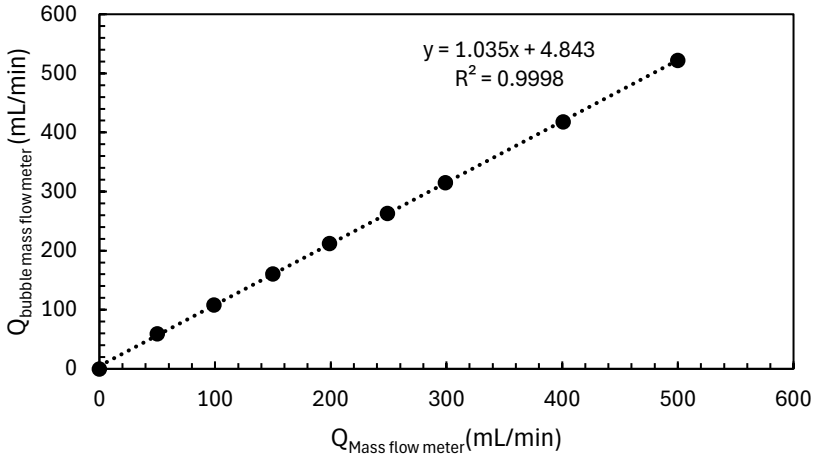

Figure 19. *Nitrogen mass flow meter calibration curve.*

3.3.2.2 TEMPERATURE MAPPING

To obtain the optimal isothermal height of the bed, the packed bed temperature was measured every 0.5 cm at different temperature set points, forming a temperature map as shown in Figure 20. The optimal height of a packed fixed bed reactor is the maximum amount of catalyst that can be added without any deviation of the temperature set pint.

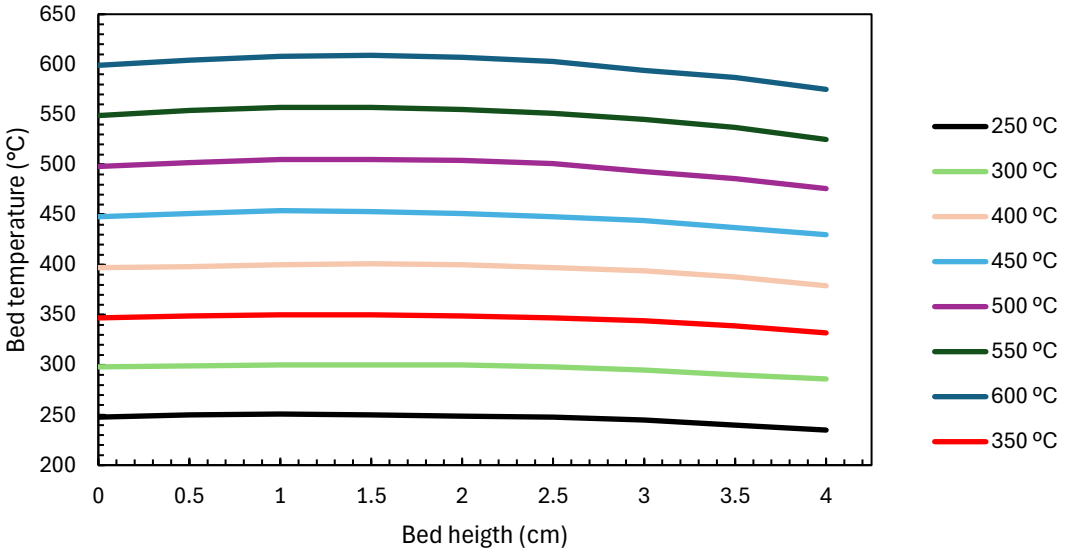

Figure 20. *Reactors bed temperature map.*

As a result of the temperature mapping of the reactor, 2.5 cm has proved to be the maximum possible bed height maintaining constant performing temperature. However, more parameters must be analysed to ensure that the height obtained from Figure 20 is the optimal one.

3.3.2.3 PARTICLE DIAMETER ESTIMATION

The flow of fluids through a packed bed generally results in a decreasing gradient of total pressure. This may produce axial change of reactant partial pressure. To ensure isobaric operation, the particle diameter must be selected in function of the following criteria(Perego and Peratello, 1999):

- The reactor diameter (D) must be at least 10 catalyst particle diameter (d_p). In this case, $\frac{D}{d_p} = \frac{1\ cm}{0.03\ cm} = s > 1$
- For gas-solid systems the catalyst bed length (L) should be at least 50 particle diameter. In this case, $\frac{L}{d_p} = \frac{2.5\ cm}{0.03\ cm} = vd > 50$

The diameter of the particle and the height of the bed ensure an isobaric operation ensuring an appropriate mass transfer inside the packed bed. Moreover, working with high temperatures in exothermic reactions facilitate the appearances of hot spots. Diluting the feed in an inert gas or substituting active solid by an inert are some of the common techniques in gas-solid reaction to avoid hot spots. In this case ammonia will be employed at 33% in Argon and silicon carbide to ensure optimum heat transfer in the packed bed.

3.3.2.4 GAS CHROMATOGRAPHER CALIBRATION

The analysis of the samples was performed in the SHIMADZU BID-2010 Plus employing an internal standard. To evaluate substances behaviour, several gas mixes have been analysed to make the calibration curves for methane and ammonia which are shown in Figures 21 and 22.

As it can be seen in Figures 21 and 22, ammonia and methane show a linear response. Furthermore, the height of the ammonia and the area of the methane are directly proportional to the concentration

of the respective substances. As a result, a correction factor was employed to evaluate ammonia decomposition, based on methane surface.

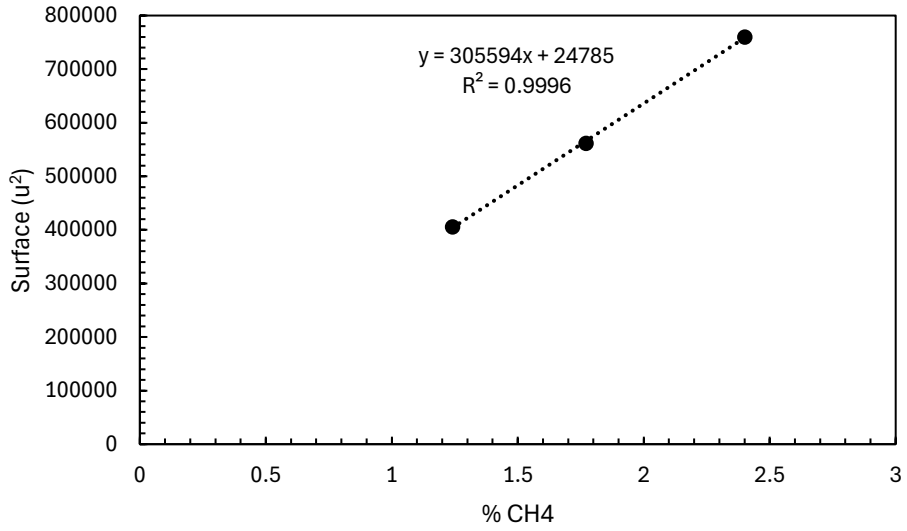

Figure 21. *Methane chromatograph calibration curve.*

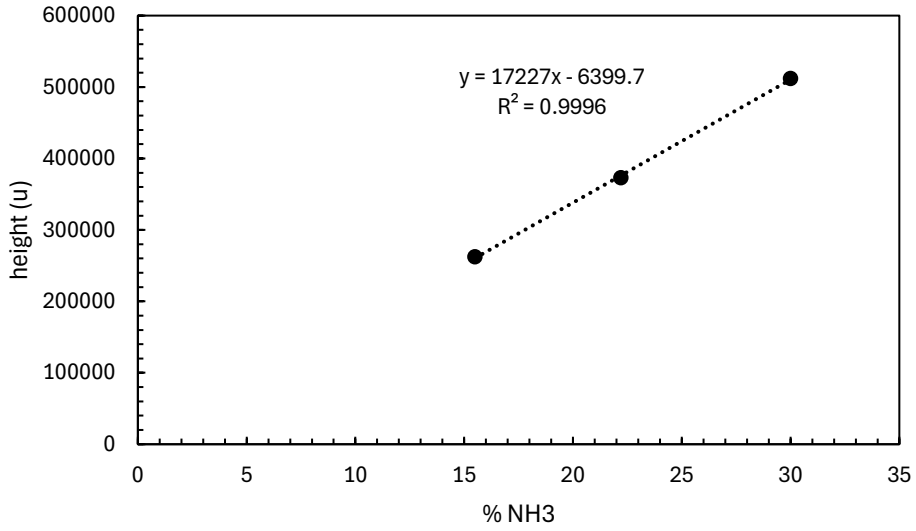

Figure 22. *Ammonia chromatograph calibration curve.*

3.3.2 REACTION

In this section the equations that were employed to calculate the conversion and hydrogen production are explained. The conversion is calculated is base of the area of the methane, for that a correction factor is calculated with Equation 14. Due to the features of the chromatographic column, it can only be measured ammonia decomposition, hydrogen and nitrogen appear under the argon peak.

$$Fr = \frac{A_i}{A_{calibration}} \tag{14}$$

The height of the ammonia pick is corrected with Equation 15.

$$H_{C,NH3} = \frac{H_{i,NH3}}{Fr} \quad (15)$$

Ammonia conversion is calculated with the height of the ammonia, the height of the ammonia feed is the average of three samples taken before starting the reaction. Ammonia conversion is calculated with Equation 16.

$$X_{NH3}(\%) = \left(\frac{H_{F,NH3} - H_{i,NH3}}{H_{F,NH3}}\right) * 100 \quad (16)$$

Hydrogen production is a parameter calculated by Equation 17. Hydrogen yield is a parameter calculated to compare catalysts activity.

$$r_{H_2}\left(\frac{mol}{gRu*s}\right) = \frac{F_{NH3} * X_{NH3} * \frac{3}{2}}{m_{Ru}} \quad (17)$$

3.4 EXPERIMENTAL METHOLOGY

To synthetize a gram of catalyst with 3% of ruthenium, 0.126 g of Ruthenium nitrosyl nitrate were dissolved in purified water, for catalysts with 1.5 % of Ruthenium 0.063 g of Ruthenium nitrosyl nitrate and for catalysts with 0.5% of Ruthenium 0.021 g of Ruthenium nitrosyl nitrate. The amount of purified water is determined by the pore volume of the support which is shown for each solid in Table 6.

Table 6. *Solvent volume calculus for each solid.*

Catalyst	Mass (g)	Pore Volume (mL/g)	Solvent Volume (mL)
3 %CeO_2	1	0.596	0.596
3 %MgO	1	0.87	0.87
3 %CeO_2	1	0.141	0.141
0.5% Ru γ-Al_2O_4	1	0.43	0.43
1.5 %$Mg_6Al_{12}(OH)_{16}CO_3H_2O$	1	0.65	0.65

All the solids were dried overnight at 100 °C to ensure complete solvent removal. For solid characterization, small quantity of solids were reduced using hydrogen at 600 °C for one hour with a ramp of 10 °C/min, except alumina that had to be calcinated before the H_2 treatment at 300 °C for one hour with a ramp of 10 °C/min. Ruthenium concertation measurement in catalysts was performed by X-rays fluorescence employing a calibration curve. Periodic structures in the catalysts were detected by X-rays diffraction in CUBIX device, and the Ru particle size was measured by STEM in JEOL Model 2100F

Catalysts were turned into a wafer employing a die and a hydraulic press. Wafers were smashed with a mortar and sieved employing 0.2 mm and 0.4 mm sieves to obtain 0.3 mm average particle diameter. The amount of catalyst added to the reactor to maintain the ammonia/ruthenium ratio constant at 37 NH_3 mL $min^{-1}mgRu^{-1}$ is shown in Table 7.

Table 7. *Catalyst reaction mass calculus.*

Catalyst	%Ru	Catalyst mass (mg)
3% $RuSiO_2$	3.11	67.52
3% $RuCeO_2$	3.29	63.83
3% RuMgO	3.21	65.42
0.5% Ru γ-Al_2O_3	0.57	368.39
1.5% Ru $Mg_6Al_{12}(OH)_{16}CO_3H_2O$	1.68	125.00

Catalysts were mixed with silicon carbide up to 2 cm of bed height and with just silicon carbide (0.6-0.8 mm) from 2 cm up to 10 cm to ensure an optimum mass and heat transfer of the feed with the bed. After gas leaks were checked, solids were reduced for 1 hour at 600 °C with a temperature ramp of 10 °C/min and after cooled down in hydrogen to 300 ° C, except alumina that previously was calcinated at 300 °C 1 hour with 10 °C/min ramp. The feed was composed by 78 mL/min of pure ammonia, 125 mL/min of internal standard and 50mL/min of argon that were stabilized thought the by-pass 15 minutes. The oven was programmed to raise the temperature to 600 °C with 2.5 °C/min. Before starting the run the samples were taken to ensure correct feed concentration.

To obtain the light-off conversion vs temperature curves, samples were taken every 8 minutes from 300° to 600 °C and analysed with the chromatograph. Once achieved 600 °C ,7 more samples were analysed to study the stability of the solids at the worst case, after the reactor was cooled down to 300 °C to perform a second light-off. After finishing the experiments, the reactor was cooled down to 400 °C with the feed and after with argon till ambient temperature. Argon was fed from two lines, ammonia line to eliminate residual ammonia in the pipeline F3 and argon of F6 line to ensure the removal of all the ammonia in the equipment. The conversion and the hydrogen production were calculated employing Equations 16 y 17.

4. RESULTS AND DISCUSSION,

4.1 SYNTHESIS RESULTS

4.1.1 X RAYS FLUORESCENCE

The calibration curves for each impregnated support, as previously mentioned in the section 3.2.1, are shown in Figures 23, 24, 25, 26 and 27. R coefficients for all the solids are very close to 1, which indirectly suggests that the experimental error is small. The correlation also shows that the response of the net rate versus ruthenium concentration is linear in the small range of concentrations investigated. For materials based on CeO_2 as the support, the calibration curve does not pass thought the origin, due to background fluorescence from this type of support.

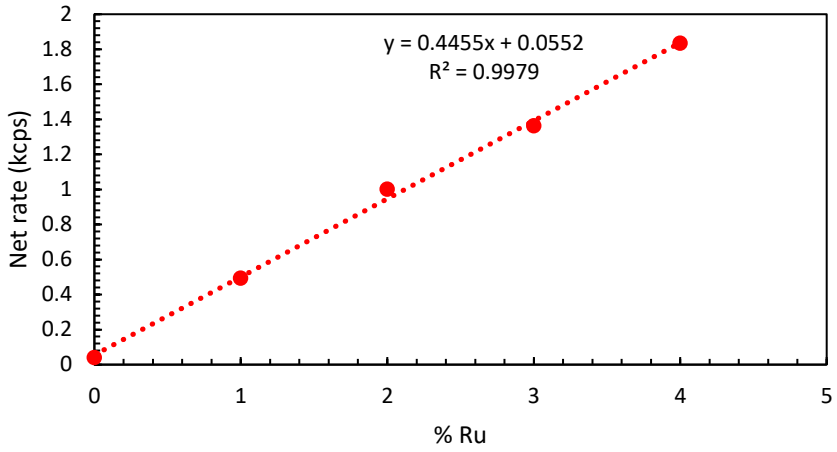

Figure 23. *Alumina fluorescence calibration curve.*

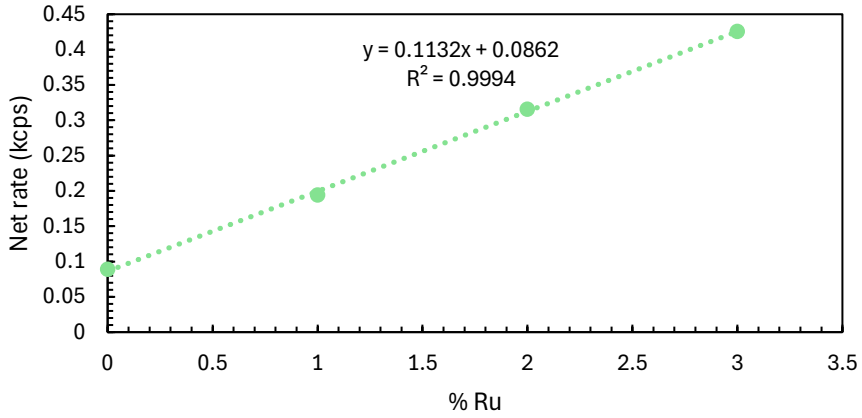

Figure 24.*Cerium oxide fluorescence calibration curve.*

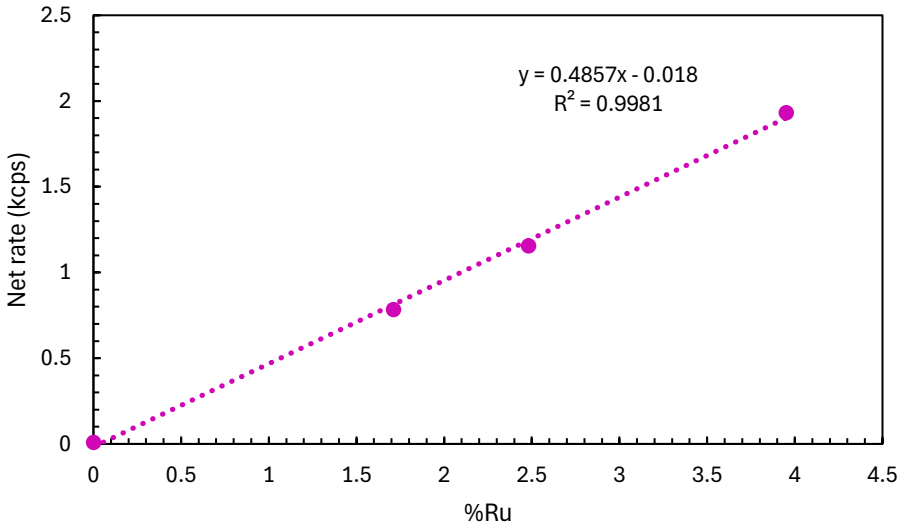

Figure 25. *Hydrotalcite fluorescence calibration curve.*

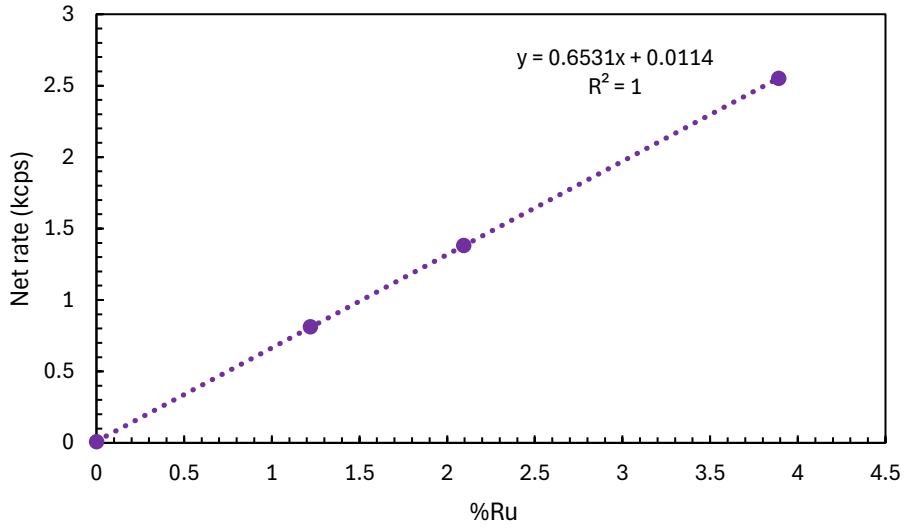

Figure 26. *Magnesium oxide fluorescence calibration curve.*

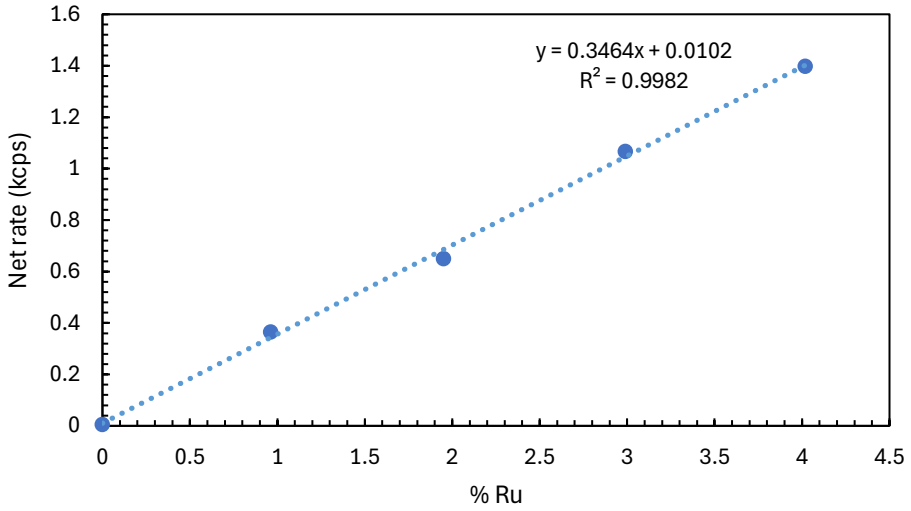

Figure 27. *Silicium oxide fluorescence calibration curve.*

Concentration results for each solid is shown in Table 8. Concentration estimation was done considering the calibration curves, as shown below. Concentrations obtained are reasonably close to nominal values targeted, catalyst mass amount must be adjusted to ensure the required conditions of 37 NH_3 mL $min^{-1}mgRu^{-1}$ which can be observed in Table 6 considering results shown in Table 8.

Table 8. *Ruthenium percentage calculated with previous calibration curves.*

Catalyst	0.5% Ru γ-Al_2O_3	3% $RuSiO_2$	3% $RuCeO_2$	3% RuMgO	1.5% Ru $Mg_6Al_{12}(OH)_{16}CO_3H_2O$
%Ru	0.57	3.11	3.29	3.21	1.68

4.1.2 XRD

In this section, the size of the Ruthenium particles and the geometry will be studied. Synthesized catalysts have been compared against their support alone, to evaluate changes that could occur during the synthesis and to detect the potential presence of large ruthenium particles. Ruthenium peaks appear at 42 degrees. STEM images will be employed to estimate particles diameter.

Figure 28 shows the diffractogram of alumina Ru 3% alone, and that of the Ru/Al_2O_3 material at 0.5% of Ru after calcination and reduction. In case of Figure 28 at angle 42 Ru peak high very high appearing shown presence of big particles, the reason with ruthenium concentration in solid was reduced to 0.5 %. Figure 29 shows small peaks which are small ruthenium particles.

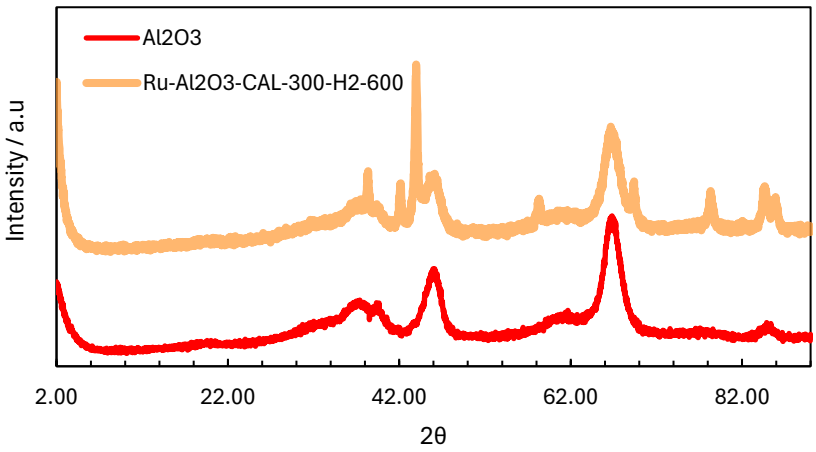

Figure 28. *Alumina support catalyst(Ru 3%) fresh diffractogram.*

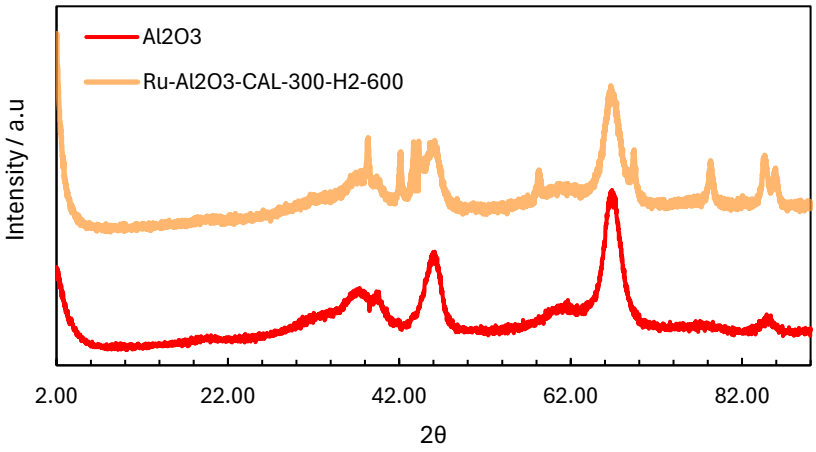

Figure 29. *Alumina support catalyst(Ru 0.5%) fresh diffractogram.*

Figures 30, 31 ,32 and 33 show the cerium oxide, magnesium oxide, hydrotalcite and silica oxide diffractograms, compared to those of the same materials loaded with 3% of Ruthenium. The absence of XRD peaks attributable to Ru indicates that clusters on all these supports are too small to be detected by this technique (smaller than ~ 5 nm). In the case of the hydrotalcite sample, the diffractogram shows a change in the crystallinity of the support, corresponding to a change from the hydrotalcite phase to the corresponding mixed metal oxides after the introduction of the Ru and calcination at a high temperature.

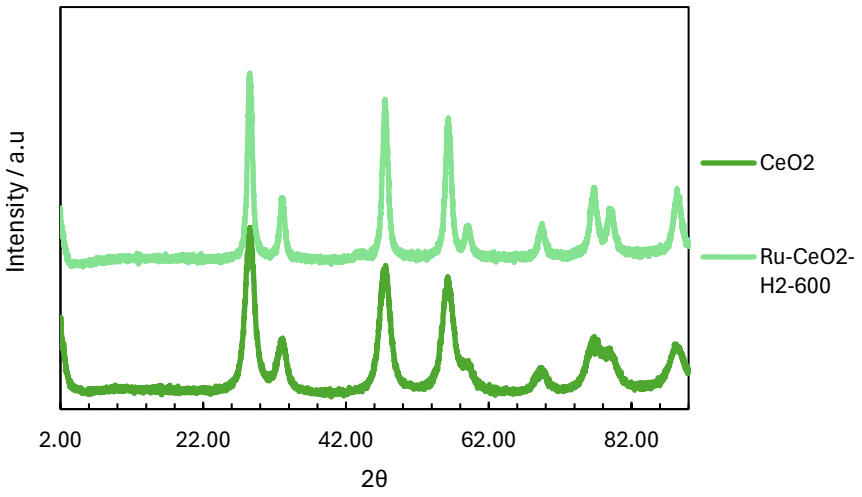

***Figure 30**.Cerium oxide support catalyst fresh diffractogram.*

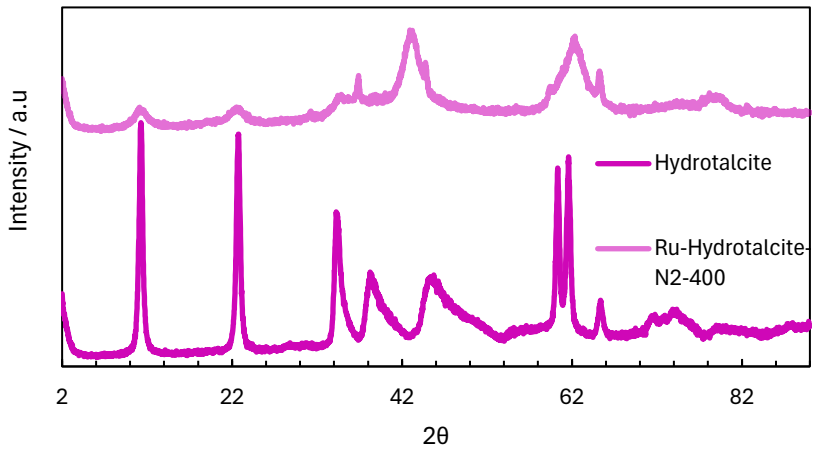

***Figure 31.**Hydrotalcite support catalyst fresh diffractogram.*

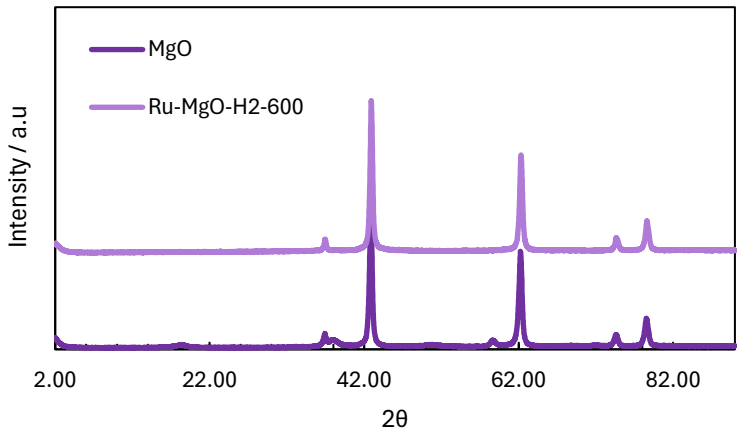

***Figure 32**.Magnesium oxide support catalyst fresh diffractogram.*

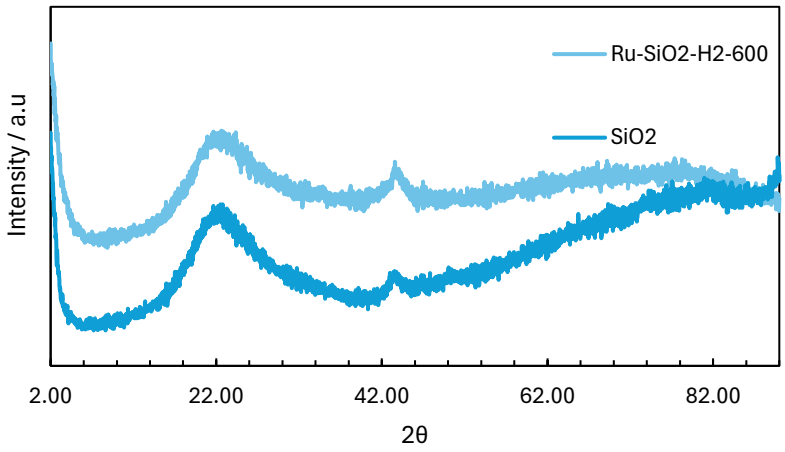

***Figure 33.** Silicium oxide support catalyst fresh diffractogram.*

4.1.3 STEM

In this section, the images obtained at different magnifications by transmission electron microscope will be explained. Images have been taken at different magnifications to evaluate the dispersion of metal clusters and the size of the particles.

Figures 34 to 38 show STEM images of the different materials synthesized in this work at three magnifications. In all cases, homogeneously distributed Ru particles of approximately 1-3 nm can be observed, consistent with the lack of XRD signals in the corresponding diffractograms. These results

fulfil one of the objectives of the project to synthesize reasonably uniform materials with approximately constant Ru particles size, to evaluate the role of the support on the catalytic performance

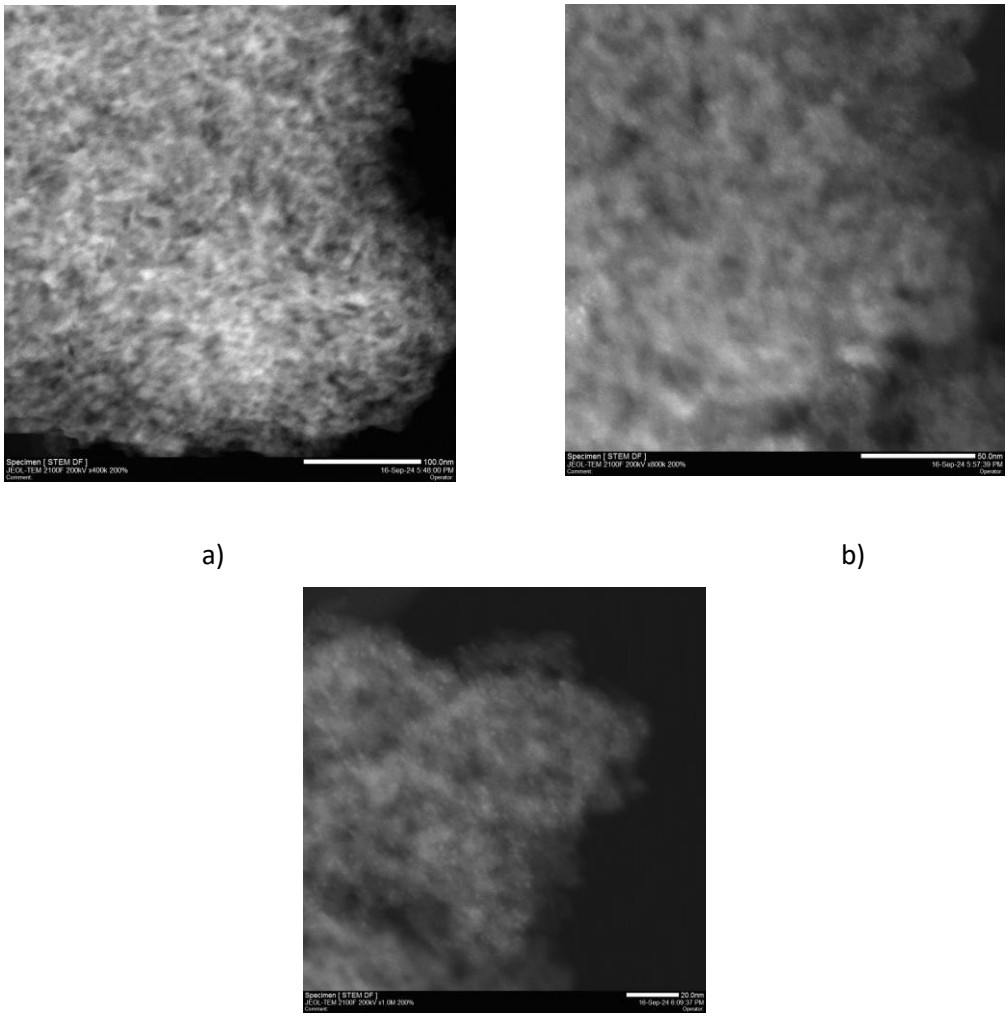

a) b)

c)

Figure 34. *STEM images for alumina-based catalysts at different magnification: a)100 nm, b)50nm and c) 20 nm.*

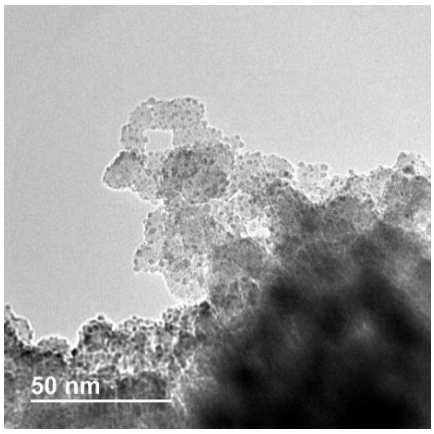

a)

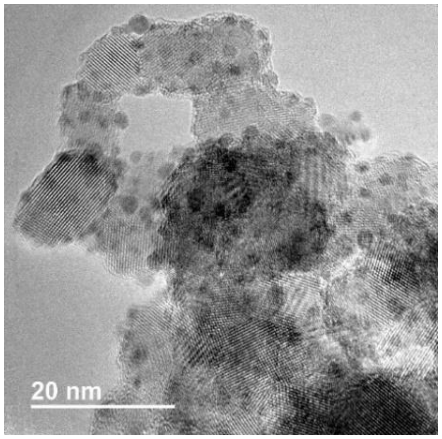

b)

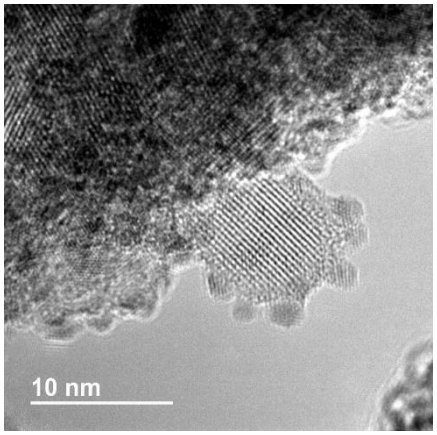

c)

Figure 35.S*TEM images for cerium oxide-based catalysts at different magnification: a)50 nm, b)20nm and c) 10 nm.*

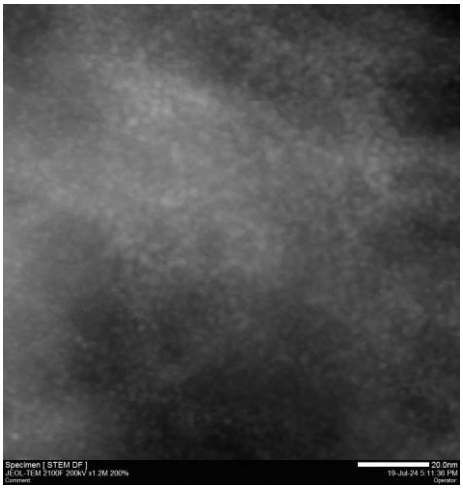

a)

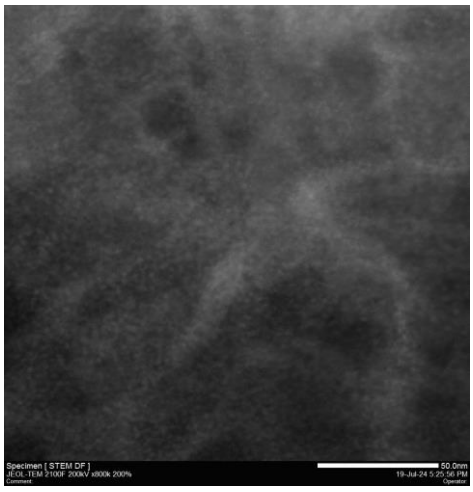

b)

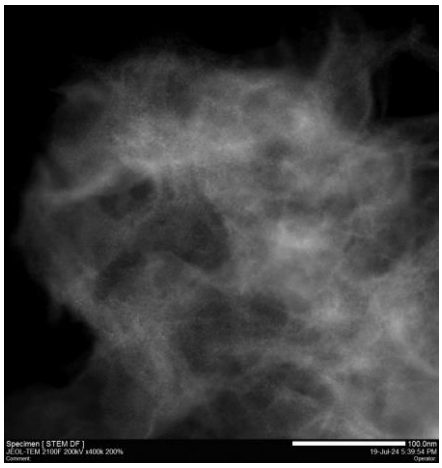

c)

Figure 36.S*TEM images for hydrotalcite-based catalysts at different magnification: a)100 nm, b)50nm and c) 20 nm.*

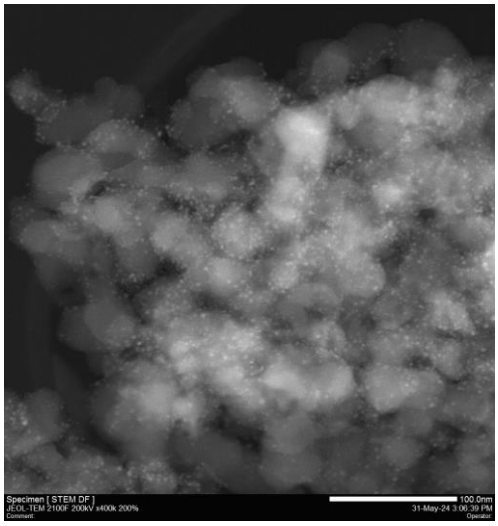

a)

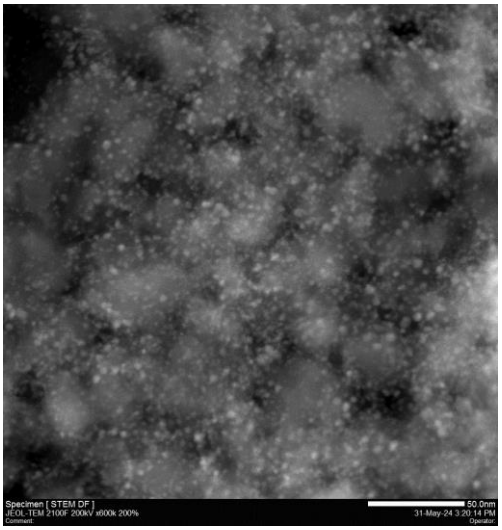

b)

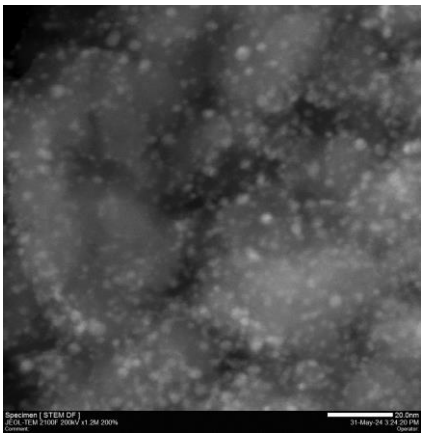

c)

Figure 37.S*TEM images for magnesium oxide catalysts at different magnification: a)100 nm, b)50nm and c) 20 nm.*

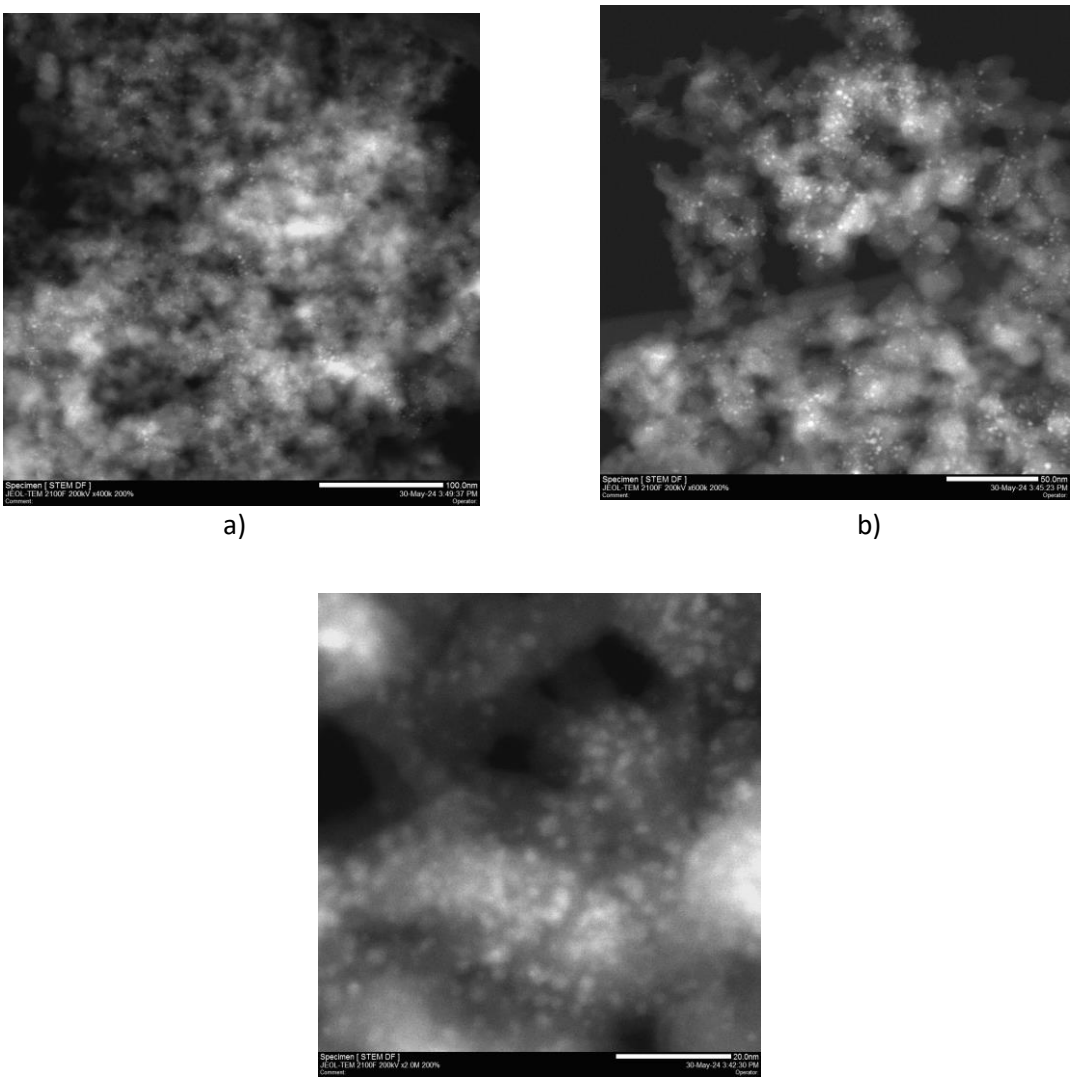

Figure 38*.STEM images for Silicium oxide-based catalysts at different magnification: a)100 nm, b)50nm and c) 20 nm.*

Table 9 summarizes the particle size inferred for the various materials from the corresponding STEM images. According to previous reports(Lee and Park, 2022), the optimal particle diameter is in between 1 and 6 nm for ammonia cracking, making the catalysts synthesized here potential good candidates.

Table 9. *Catalysts range diameter of ruthenium particles.*

Support	Particle diameter range (nm)
SiO_2	1.4-2.6
MgO	1.5-3.7
CeO_2	2.1-2.7
γ-Al_2O_4	1.5-3.3
$Mg_6Al_{12}(OH)_{16}CO_3H_2O$	2.3-3.1

4.2 CATALITIC TEST RESULTS

4.2.1 CATALYTIC PERFORMANCE

Before testing the catalysts, a thermic reaction must be performed to determine the background activity using silicon carbide as the catalyst diluent. As it can be seen in Figure 39, ammonia shows negligible activity even at the highest performing temperature, so it is assumed that the activity in the catalytic experiments will be due to the effect of the catalysts.

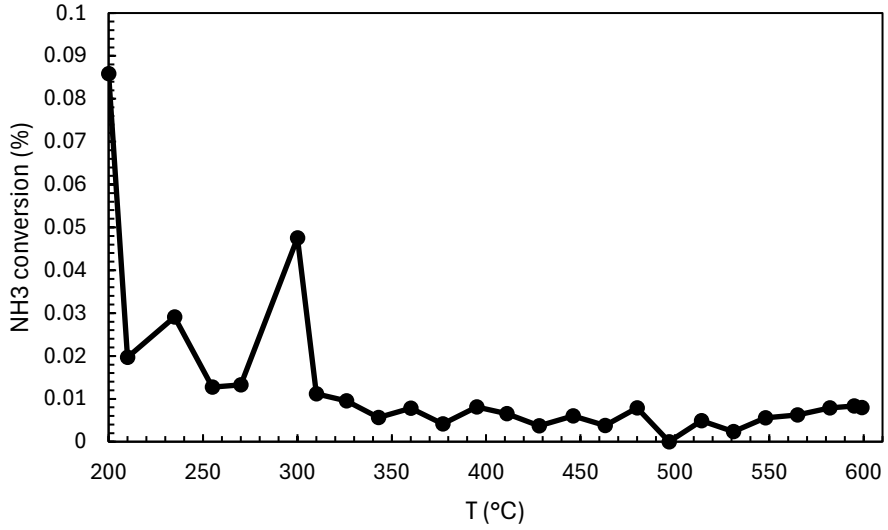

Figure 39. *Ammonia conversion evolution in a fix bed reactor between 200 °C to 600 °C. Reaction conditions: feed composition (33 mol% NH_3,*

63.6 mol% Ar, and 3.4 mol% CH_4),

Once the activity of the silicon carbide with the temperature had been investigated, the activity of the various catalyst was investigated through light off "conversion vs temperature "experiments, shown in Figure 40. In these runs, Ru on magnesium oxide and silica oxide provide the highest ammonia conversion at a given temperature and reach 100 % conversion at the highest temperature investigated (~100 %). Ru on hydrotalcite and ceria, on the other hand, provide intermediate levels of activity, and Ru on alumina appears to be the least active material (Figure 40). Interestingly, whereas the hydrotalcite and ceria curves show simply shifted to the right compared to MgO and SiO_2, the Ru/Al_2O_3 curve slows down more pronouncedly as the reaction temperature increases. To understand these results more in detail, new experiments were designed that evaluate the stability of the various catalysts under reaction conditions.

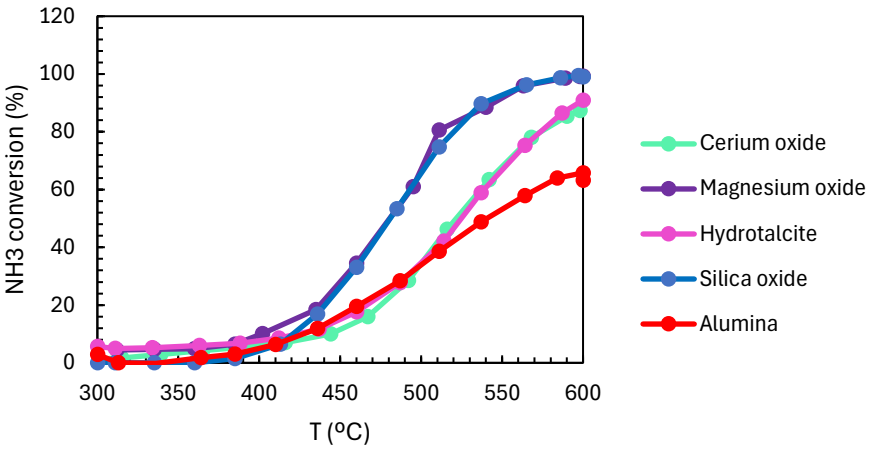

Figure 40. *Ammonia conversion evolution comparison between the studied catalysts in a fix bed reactor between 200 °C to 600 °C. Reaction conditions: feed composition (33 mol% NH_3,63.6 mol% Ar, and 3.4 mol% CH_4),*

4.2.2 CATALYTIC STABILITY

Catalytic stability measures the capacity of catalysts to sustain their performance (e.g. activity) constant over time as exposed to specific reaction conditions. A practical way to evaluate the catalytic stability is to compare the "conversion vs temperature" plot of fresh catalysts and spent catalysts (referred here as "1 light off" and "2 light off"). The second light off curves were obtained after holding the materials at 600ºC in the reaction mixture for 60 minutes. Figure 40 shows the activity of each catalyst over time at this highest temperature, prior to collection of the second light off curve. Ru/MgO and Ru/SiO_2 show full conversion of ammonia at 600ºC during this period, whereas Ru/Hydrotalcite shows near constant conversion at ~ 90 %. Finally, Ru/CeO_2 and, specially, Ru/Al_2O_3 show some symptoms of deactivation.

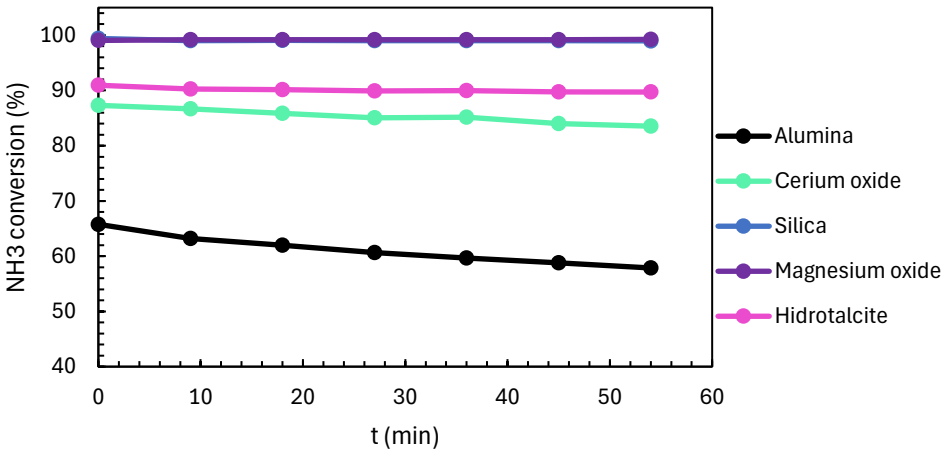

Figure 41.*Catalysts stability test comparison. Reaction conditions: feed composition (33 mol% NH_3,63.6 mol% Ar, and 3.4 mol% CH_4),*

Figure 42 through 46 compare the "conversion vs temperature" plots for all these catalysts in back-to-back experiments. Consistent with the isothermal results, the light off curve of Ru on Al_2O_3 shifts the

most to higher temperatures after the first use, followed by Ru/CeO_2 and then, rest of the catalysts, which barely lose activity after being aged.

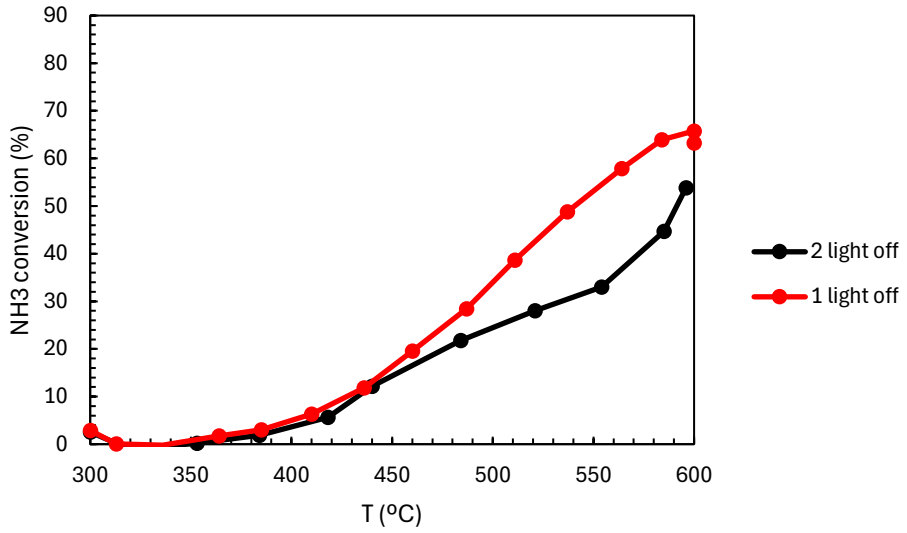

Figure 42. *Alumina comparison between first and second light-off. Reaction conditions: feed composition (33 mol% NH_3, 63.6 mol% Ar, and 3.4 mol% CH_4),*

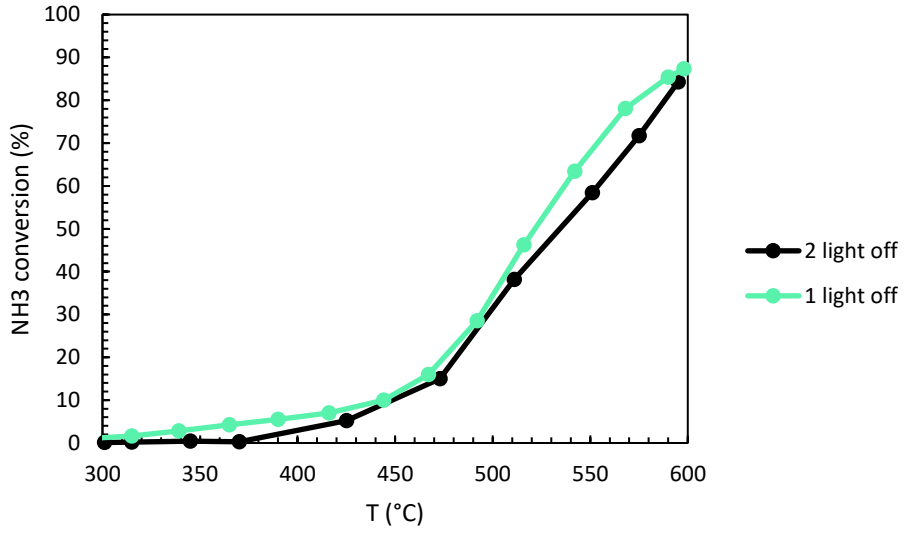

Figure 43. *Cerium oxide comparison between first and second light-off. Reaction conditions: feed composition (33 mol% NH_3, 63.6 mol% Ar, and 3.4 mol% CH_4),*

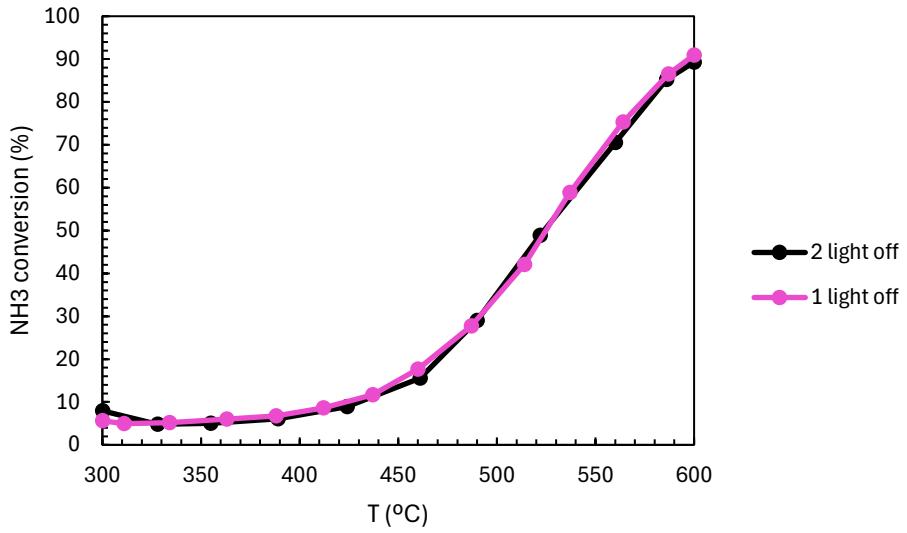

Figure 44.*Hydrotalcite comparison between first and second light-off. Reaction conditions: feed composition (33 mol% NH_3, 63.6 mol% Ar, and 3.4 mol% CH_4),*

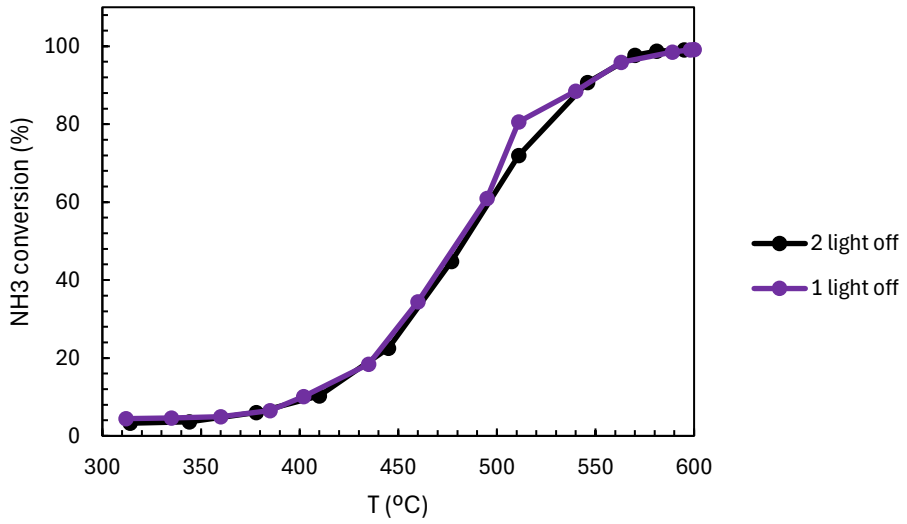

Figure 45. *Magnesium oxide comparison between first and second light-off. Reaction conditions: feed composition (33 mol% NH_3,63.6 mol% Ar, and 3.4 mol% CH_4),*

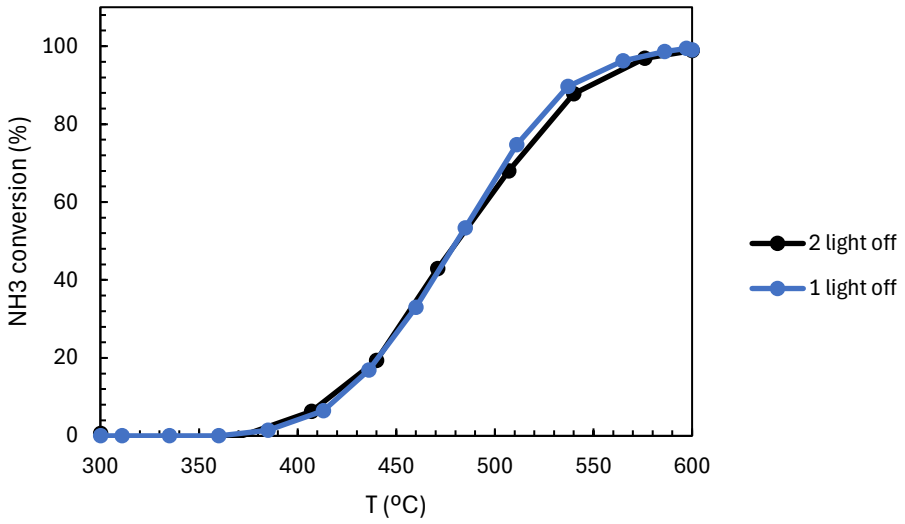

Figure 46. *Silicium oxide comparison between first and second light-off. Reaction conditions: feed composition (33 mol% NH_3,63.6 mol% Ar, and 3.4 mol% CH_4)*

4.2.3 HYDROGEN PRODUCTION

Hydrogen production is a crucial parameter for developing hydrogen carriers. It reports the amount of hydrogen generated in each reaction. Therefore, it reports indirect economical perspective of the reaction. Silica oxide is the solid with the highest hydrogen production due to the high superficial area that possesses. Observing STEM images in Figure 37, metal clusters in Silica oxide are very dispersed increasing the active area of the catalyst. Alumina is the following, but this solid studied cannot be considered due to the low activity of the catalyst. Comparing Hydrotalcite, Magnesium oxide and Cerium oxide the acidity of the material is inversely proportional to the hydrogen production. Hydrotalcite is the material with hydrogen production between Cerium oxide and Magnesium oxide due to the amphoteric behaviour.

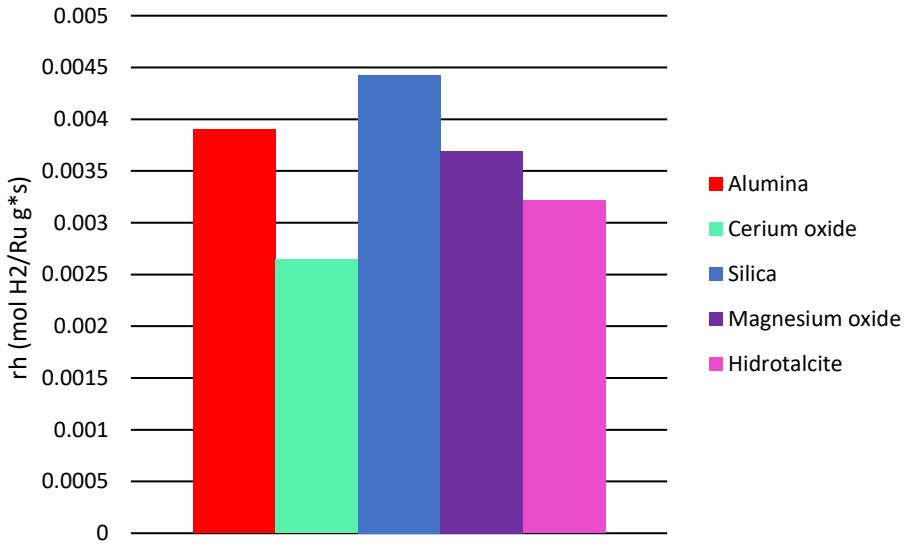

Figure 47.*Hydrogen comparison between the catalysts at 417 °C. Reaction conditions: feed composition (33 mol% NH_3, 63.6 mol% Ar, and 3.4 mol% CH_4).*

4.2.4 POST REACTION CHARACTERIZATION

In this section, the characterization of reused catalysts is discussed, using XRD and STEM. These tests aim at detecting potential changes in the size of the Ruthenium particles because of their exposure to the harsh reaction conditions in this investigation.

4.2.4.1 X RAYS DIFFRACTION POST-REACION

Figure 48 through 52 show the diffractogram comparison between the fresh materials and the post-reaction materials. All the Figures are very similar, except Figure 52 that shows at 42° that represents high particle diameter. Furthermore, there are several peaks in other angles that appear only in post reaction diffractogram which belong to Silicon carbide and possible contaminated particles in the sample.

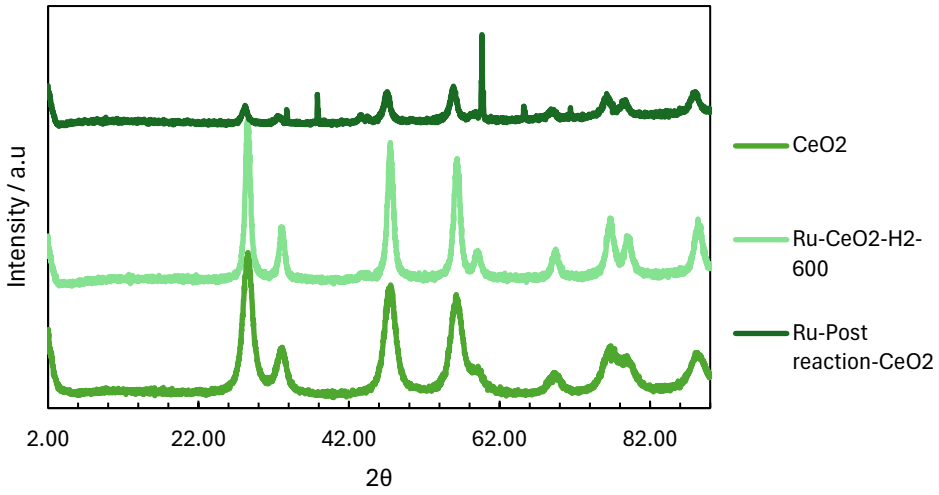

Figure 48. *Fresh Cerium oxide and reused comparison diffractogram.*

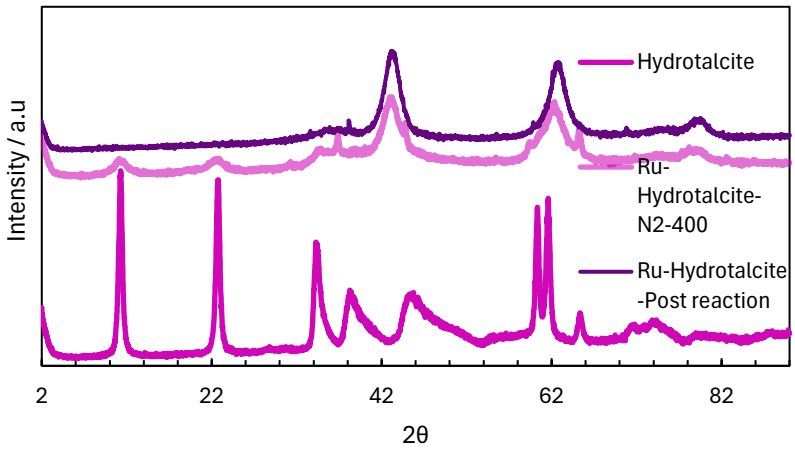

Figure 49. *Fresh Hydrotalcite and reused comparison diffractogram.*

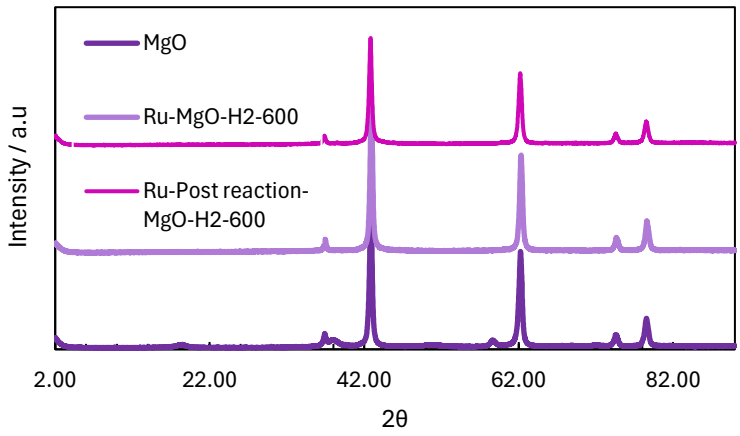

Figure 50.*Fresh Magnesium oxide and reused comparison diffractogram.*

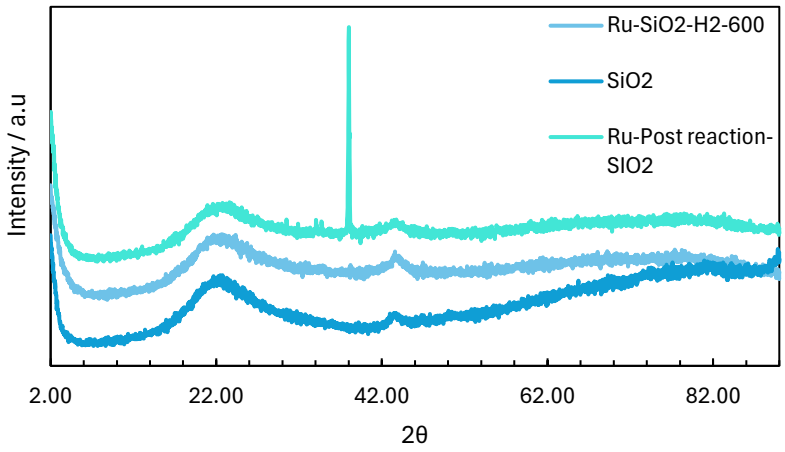

Figure 51.*Fresh Silica and reused comparison diffractogram.*

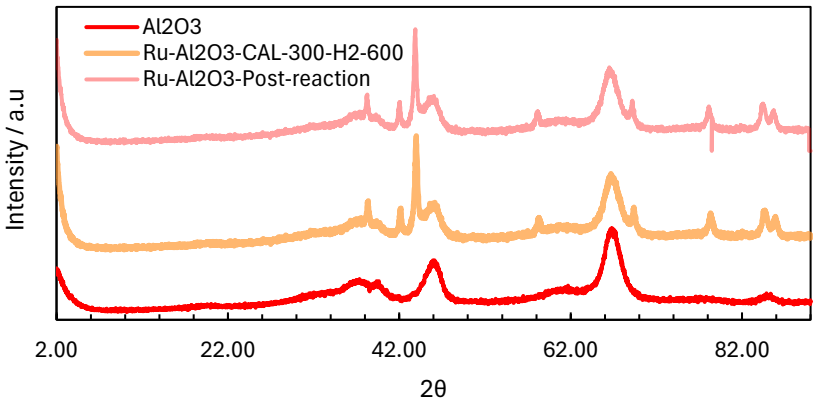

***Figure 52**.Fresh alumina and reused comparison diffractogram.*

4.2.4.2 TRANSMISION ELECTRON MICROSCOPE

The spent catalysts were also analysed by STEM. Roughly speaking, changes in the Ru particle size and/or distribution after reuse of the catalysts are minimal when the support is MgO, CeO_2, hydrotalcite or SiO_2. In general, these materials retain Ru in the form of small nanoparticles of 2-6 nm after their exposure to ammonia at 600ºC (Figures53, 54,55, 56 and 57), consistent with the previous XRD results. In sharp contrast, Ru shows evident agglomeration into large metal nanoparticles (Figure 53), matching the presence of XRD signal 42 angles in Figure 47. Particle size distributions of spent catalysts are summarized in Table 10

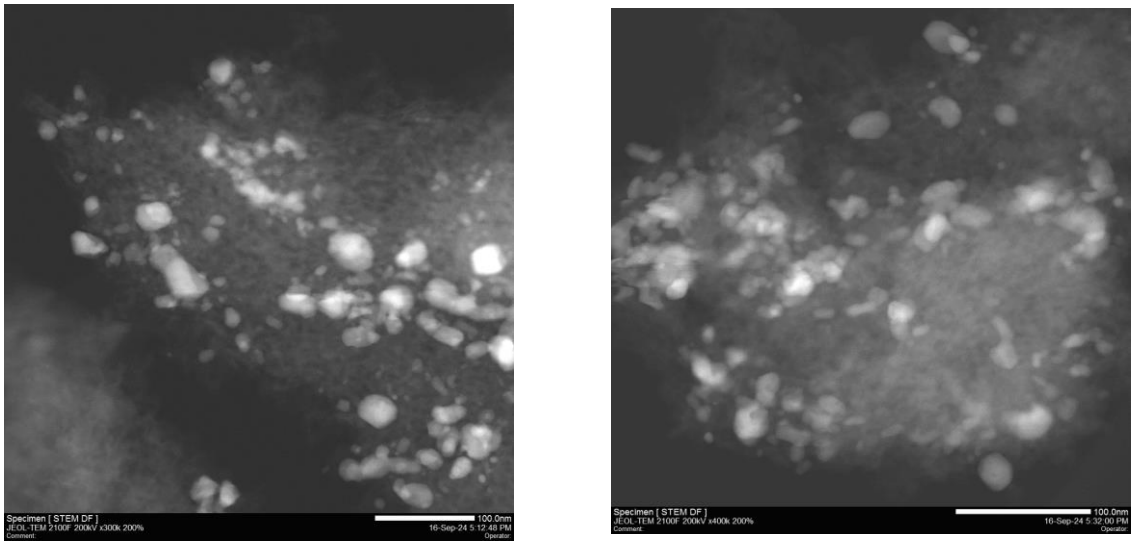

a) b)

***Figure 53.** Alumina Post-reaction STEM images with same magnification and different positions.*

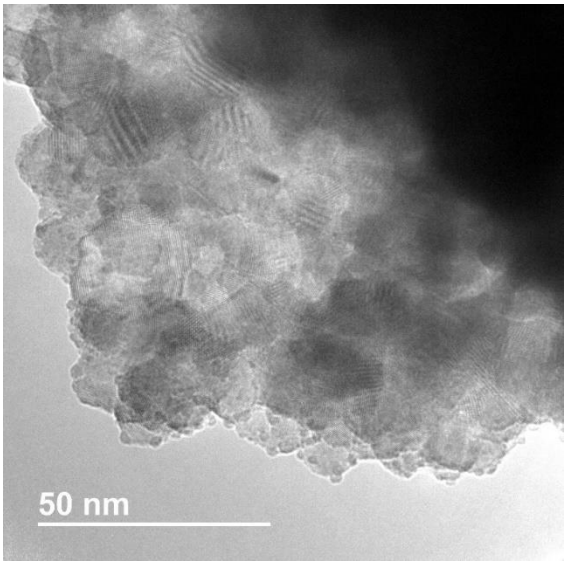

a)

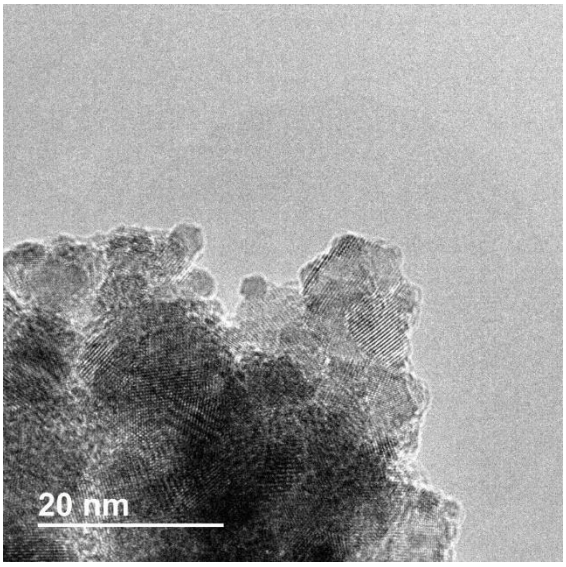

b)

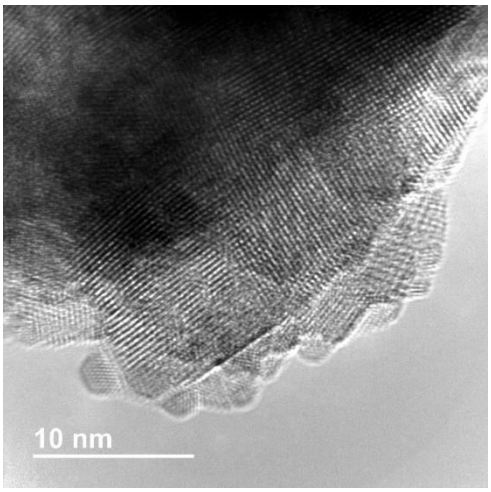

c)

***Figure 54**.Cerium oxide Post-reaction STEM images: a) 50 nm, b) 20 nm and c) 10 nm.*

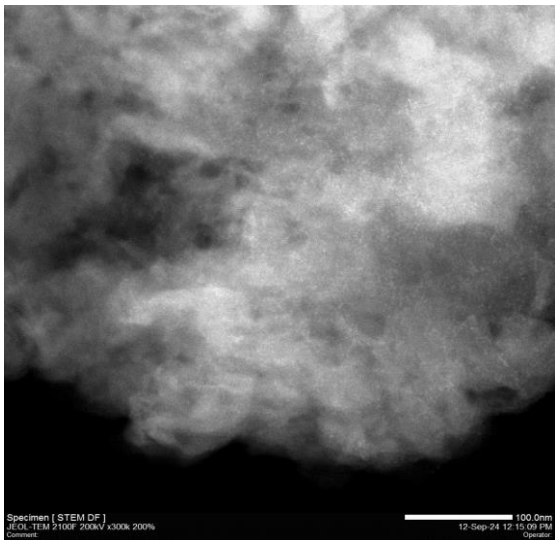

a)

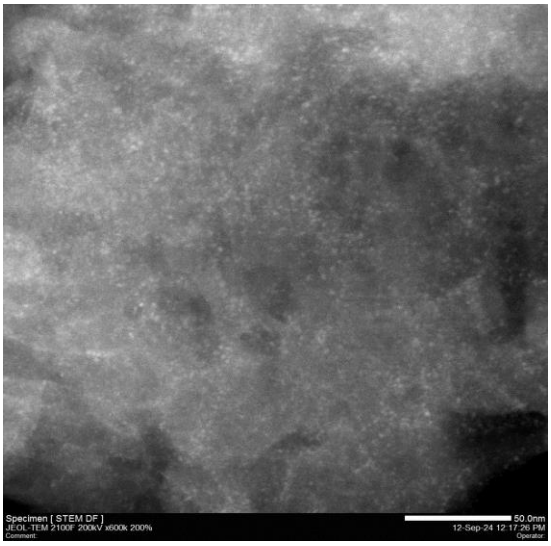

b)

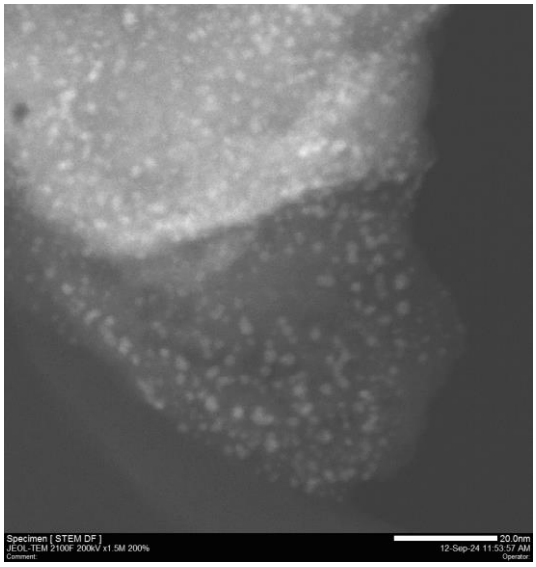

c)

Figure 55.*Hydrotalcite Post-reaction STEM images: a) 100 nm, b) 50 nm and c) 20 nm.*

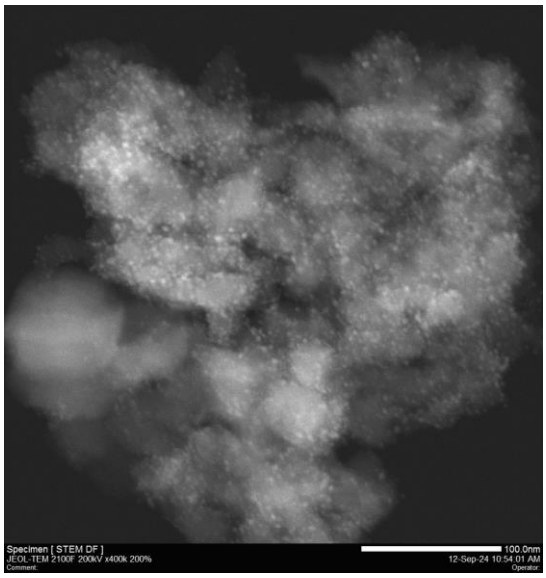

a)

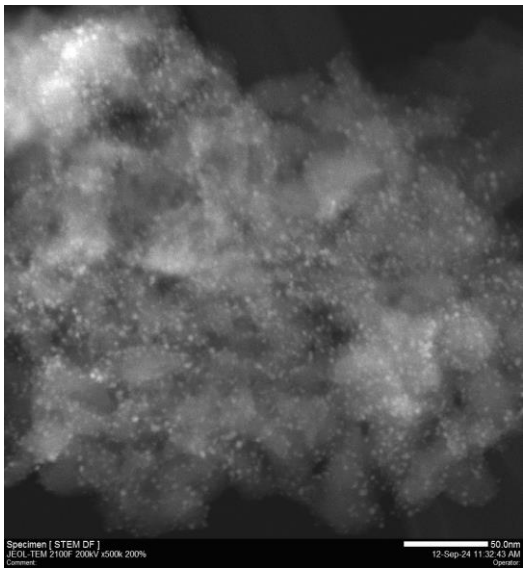

b)

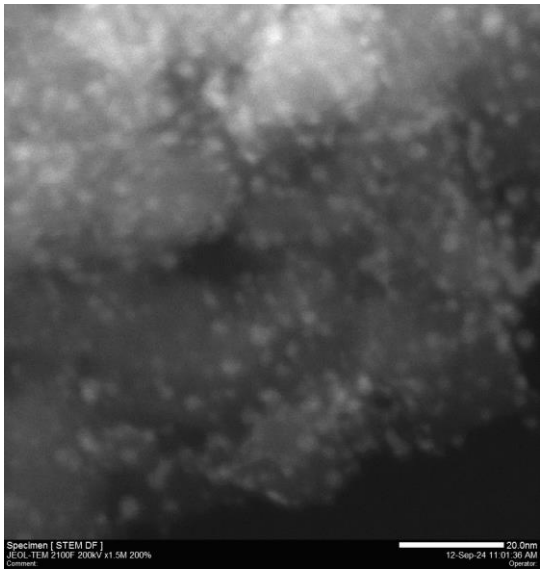

c)

Figure 56.*Magnesium oxide Post-reaction STEM images: a) 100 nm, b) 50 nm and c) 20 nm*

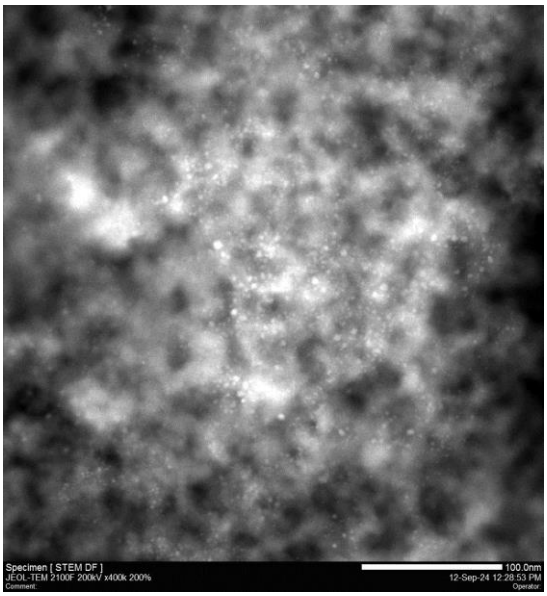

a)

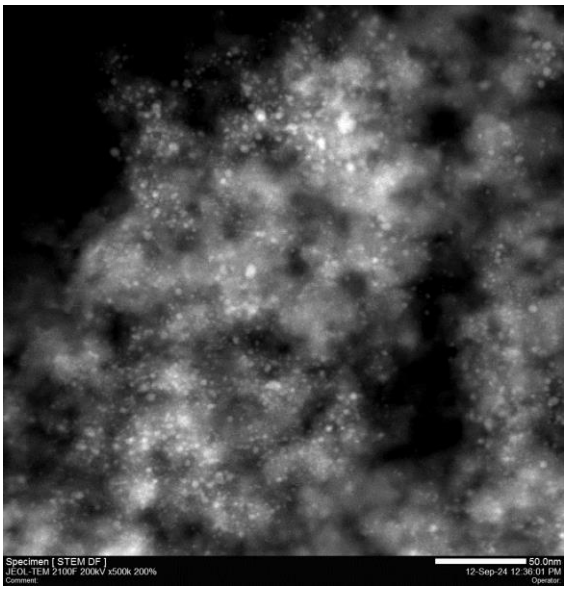

b)

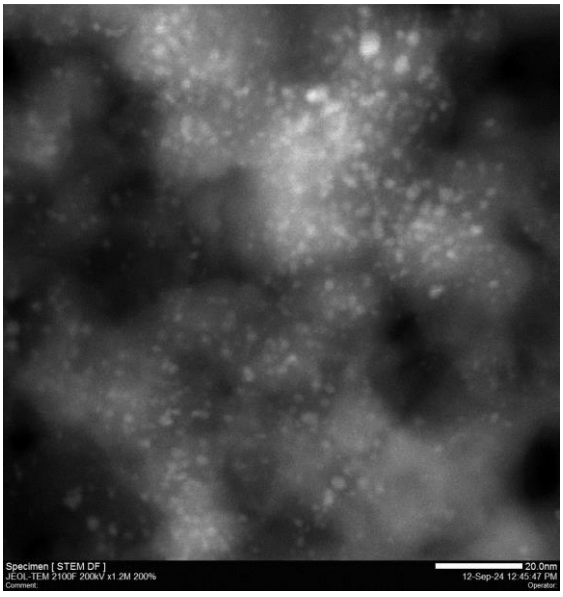

c)

***Figure 57**.Silica oxide Post-reaction STEM images: a) 100 nm, b) 50 nm and c) 20 nm.*

Table 10 summarises the range of diameters of post reaction catalyst. As explained before the catalysts which suffered deactivation, have higher diameters range whereas the stable solids diameter range remains similar compared to the fresh material.

Table 10. *Post reaction materials particle size range.*

Support	Particle diameter range (nm)
SiO_2	1.4-2.6
MgO	1.5-3.7
CeO_2	3,5-6,4
γ-Al_2O_4	20-50
$Mg_6Al_{12}(OH)_{16}CO_3H_2O$	2.3-3.1

4.2.5. STRUCTURE-PERFORMANCE CORRELATIONS

The catalysts synthesized in this work contain Ru nanoparticles in a narrow particle size range, regardless of the nature of the support. Preliminary optimization of the synthesis methods was necessary to achieve these results, after testing various Ru precursors and activation methods (not shown in this report). Our data strongly suggests that particle size is an insufficient descriptor of catalytic activity in ammonia cracking, since Ru on CeO_2, Al_2O_3 and hydrotalcite are substantially less active than on MgO and SiO_2. The particular low activity of Ru on alumina seems to be associated with the high mobility of the metal in mixture of ammonia/H_2, which leads to aggregation of the metal and loss of effective area for the catalysis.

From an electronic perspective, supports that include Lewis's acidity, such as CeO_2, hydrotalcite, and Al_2O_3, appear to have a detrimental effect over the catalytic activity, but additional work would be needed to investigate these effects more in detail. In light of the results, indeed, an argument that other properties may play important roles in the cracking of ammonia can be made, since MgO and SiO_2, with notably different acid/base characteristics, provide similar results. It is interesting to observe that Ru can be made as small nanoparticles using a weakly interacting support such as SiO_2, offering unanticipated activity and stability.

5.CONCLUSIONS

Ammonia cracking is a plausible alternative for green hydrogen production in countries with poor renewable electrical production. In this work, we have investigated Ruthenium-based catalysts for ammonia cracking, considering literature precedents showing its high activity relative to other transition metals.

We show that catalysts can be successfully synthesized by wetness impregnation to yield small metal nanoparticles of 2-3 nm on various types of supports, including SiO_2, CeO_2, MgO, Al_2O_3, and hydrotalcite. The use of ruthenium nitrosyl nitrate as the Ru precursor is shown critical to obtain these results, with H_2 catalyst activation as the only thermal treatment required to form the metal nanoparticles. RuACAC and $RuCl_3$ have been employed but they present the following problems: $RuCl_3$ is difficult to dissolve correctly and RuACAC felt down in calcination reactor.

Alumina is the only material that requires calcination before hydrogenation. In case of alumina, calcination increases metal cluster dispersion and posterior hydrogenation to reduce particle size. The rest of materials only required hydrogenation due to the features of the support and metal precursor. Transmission electron microscopy, X rays fluorescence and X rays diffraction was used to measure concentration of Ruthenium in each catalyst and the size of metal clusters.

Reaction equipment was set up correctly, adding a manometer and a valve to GC inlet to avoid over pressure. EPDM is a suitable material to employ in any pipeline for ammonia, due to the resistance to ammonia corrosion avoiding ammonia leaks. On the other hand, experimental errors during the calibrations were minimized, employing bubble calibrated flow meter. R coefficient of all the calibration curves was found to be close to 1. Gas chromatograph calibration was performed correctly obtaining a linear response of the equipment.

From the catalysts studied Silica oxide and Magnesium oxide have the highest activity. In case of the Silica oxide, higher superficial area and correctly dispersed metal cluster increase the activity despite of been neutral makes it the most active one, whereas magnesium oxide having half of superficial area, the electron giving behaviour balances having lower superficial area. Acid/ Base behaviour is more relevant than superficial area, the activity is inversely proportional to de acidity of the support and directly proportional to the superficial area. Finaly as hydrogen production is directly proportional to the conversion, follows the previous statement. It is possible to achieve high conversions between 400°C and 500 °C.

From the economic point of view, there is no big difference between the catalysts. Support cost is the parameter that variates between the solids. The rest of parameters are similar in energetic requirements or characterization costs.

In relation with the Sustainable Development Goals, this research has proved to improve the following goals 7, 9, 11, 12 and 13. Facilitating green hydrogen to countries with poor renewable energy, reduces carbon dioxide emissions, develops the industry, developing cities sustainability and promotes the circular economy increasing responsible consumption and production.

In my opinion this work should be further developed in the following matters: Ruthenium concentration study over magnesium oxide needs to be done to evaluate the size, shape and dispersion of the metal clusters for different concentrations and controlling the size and dispersion of particles by calcination and hydrogenation. From the reaction point of view: different especial velocities, study of preheating and study the activity for very low ammonia concentrations.

6. NOMENCLATURE

A Peak surface

C Space light speed

D Diameter

F Molar flow

H Peak height

h Planck´s constant

I Intensity

L Reactor length

M Mass; Molar mass

P Partial pressure

T Temperature

U Cell voltage

V Absorbed volume

X Conversion

Z Exchanged electrons

Subscripts

In

Out

Greek symbols

θ diffraction angle

λ wavelength

μ attenuated electrons

τ absorption coefficient

7. BIBLIOGRAPHY

AMMONIA TRANSPORT &, n.d.

Ball, M., Wietschel, M., 2009. The future of hydrogen - opportunities and challenges. Int. J. Hydrogen Energy 34, 615–627. https://doi.org/10.1016/j.ijhydene.2008.11.014

Brauns, J., Turek, T., 2020. Alkaline water electrolysis powered by renewable energy: A review. Processes 8. https://doi.org/10.3390/pr8020248

Brito, R.C., Béttega, R., Freire, J.T., 2019. Energy analysis of intermittent drying in the spouted bed. Dry. Technol. 37, 1498–1510. https://doi.org/10.1080/07373937.2018.1512503

Chen, C., Wu, K., Ren, H., Zhou, C., Luo, Y., Lin, L., Au, C., Jiang, L., 2021. Ru-Based Catalysts for Ammonia Decomposition: A Mini-Review. Energy and Fuels 35, 11693–11706. https://doi.org/10.1021/acs.energyfuels.1c01261

Climent, M.J., Corma, A., Iborra, S., Epping, K., Velty, A., 2004. Increasing the basicity and catalytic activity of hydrotalcites by different synthesis procedures. J. Catal. 225, 316–326. https://doi.org/10.1016/j.jcat.2004.04.027

Diffraction, X.P., n.d. X-RAY POWDER DIFFRACTION XRD for the analyst X-RAY POWDER DIFFRACTION XRD for the analyst.

Fang, H., Wu, S., Ayvali, T., Zheng, J., Fellowes, J., Ho, P., Leung, K.C., Large, A., Held, G., Kato, R., Suenaga, K., Reyes, Y.I.A., Thang, H.V., Chen, H.T., Chi, S., Tsang, E., 2023. Dispersed surface Ru ensembles on MgO (111) for catalytic ammonia decomposition. https://doi.org/10.1038/s41467-023-36339-w

García, A., García, L., López, E., Becerra, N., Ojeda, I., 2010. Reformado auto-térmico de metano con CO 2 , vapor y O 2 a gas de síntesis , sobre catalizadores estructurados basados en perovskitas.

Global Hydrogen Review 2021, 2021. . Glob. Hydrog. Rev. 2021. https://doi.org/10.1787/39351842-en

Lee, H.J., Park, E.D., 2022. Ammonia Decomposition over Ru / SiO 2 Catalysts 1.

Moussa Martí, S., 2020. Desarrollo de catalizadores bifuncionales basados en Ni disperso en aluminosilicatos porosos ácidos para la oligomerización heterogénea de etileno.

Panwar, N.L., Kaushik, S.C., Kothari, S., 2011. Role of renewable energy sources in environmental protection: A review. Renew. Sustain. Energy Rev. 15, 1513–1524. https://doi.org/10.1016/j.rser.2010.11.037

Perego, C., Peratello, S., 1999. Experimental methods in catalytic kinetics. Catal. Today 52, 133–145. https://doi.org/10.1016/S0920-5861(99)00071-1

Rasool, M.H., Ahmad, M., Ayoub, M., 2023. Selecting Geological Formations for CO2 Storage: A Comparative Rating System. Sustain. 15, 1–39. https://doi.org/10.3390/su15086599

Report, A.D.I., 2022. 【】2022中国素质教育行业报告 2022. 多鲸资本 6, 1–8.

Sims, R.E.H., Senelwa, K., Maiava, T., Bullock, B.T., 1999. Eucalyptus species for biomass energy in New Zealand - Part II: Coppice performance. Biomass and Bioenergy 17, 333–343. https://doi.org/10.1016/S0961-9534(99)00043-4

Spatolisano, E., Pellegrini, L.A., Angelis, A.R. De, Cattaneo, S., Roccaro, E., 2023. Ammonia as a Carbon-Free Energy Carrier : NH 3 Cracking to H 2. https://doi.org/10.1021/acs.iecr.3c01419

Sun, Y., Welch, G.C., Leong, W.L., Takacs, C.J., Bazan, G.C., Heeger, A.J., 2012. Solution-processed small-molecule solar cells with 6.7% efficiency. Nat. Mater. 11, 44–48. https://doi.org/10.1038/nmat3160

Wattanakit, C., Corma, A., Catalysis, H., Mizuno, T., Operation, K., n.d. ChemCatChem The influence of additives derived from zeolite / LDH composites on catalytic cracking of heavy petroleum oils for light olefin production .

Yang, H., Ye, H., Zhai, S., Wang, G., 2011. Leak detection of gas transport pipelines based on wigner distribution. 2011 Int. Symp. Adv. Control Ind. Process. 258–261. https://doi.org/10.1002/apj

Zainal, B.S., Ker, P.J., Mohamed, H., Ong, H.C., Fattah, I.M.R., Rahman, S.M.A., Nghiem, L.D., Mahlia, T.M.I., 2024. Recent advancement and assessment of green hydrogen production technologies. Renew. Sustain. Energy Rev. 189, 113941. https://doi.org/10.1016/j.rser.2023.113941

Zhang, J., Hao, S., Jiang, D., Huan, Y., Cui, L., Liu, Y., Yang, H., Ren, Y., 2017. In situ synchrotron high-energy X-ray diffraction study of microscopic deformation behavior of a hard-soft dual phase composite containing phase transforming matrix. Acta Mater. 130, 297–309. https://doi.org/10.1016/j.actamat.2017.03.052

Zhu, B., He, S., Yang, Y., Li, S., Lau, C.H., Liu, S., Shao, L., 2023. Boosting membrane carbon capture via multifaceted polyphenol-mediated soldering. Nat. Commun. 14. https://doi.org/10.1038/s41467-023-37479-9

BUDGET

1.1. COSTS DEFINITION

In this part, all the reactants, devices, energy and resources employed in the research costs are defined. Defining first the costs helps understanding the total costs of each catalyst. Reactants cost is shown in Table 1; Characterization cost is shown in Table 2; Energy cost shown in Table 3 and human resources costs in Table 4.

***Table 1**. Material resources cost resume.*

Materials	Magnitude	Price (€/unit)
Precursor RuNONO2	g	71.8
Purified water	ml	3.E-06
Magnesium oxide	g	0.37
Gamma alumina	g	0.55
Hydrotalcite	g	0.12
Cerium oxide	g	0.67
Silica oxide	g	2.23
Hydrogen	ml	1.66258E-05
Argon	ml	5.41458E-05
Nitrogen	ml	5.79589E-05
Internal Standard	ml	2.23402E-05
Ammonia	ml	7.87636E-05
Helium	ml	3.32517E-05

***Table 2.** Characterization technique cost resume.*

Characterization technique	Price (€/ sample)
X-rays fluorescence	31.64
TEM Microscopy	77.11
X-Rays diffraction	64.93

***Table 3.** Energetic resource cost resume.*

Device	Power (kW)
Drying oven	0.5
Calcination oven	1
Reduction oven	1
Reactor oven	0.45

***Table 4.** Human resources cost resume.*

Resource name	Hour cost (€/h)
Javier	9.5
Benjamin	12
Aroa	15
Pedro	20
Cristina	20

1.2. ECONOMIC EVALUATION OF EXPERIMENTATION

In this section will be analysed the reaction cost of all the catalyst that have been examined in this work. Tables 5 ,6, 7, 8 and 9 show the economic cost of each resource employed for each material, comparing the total cost of the materials

*T**able 5**. Alumina catalytic test total cost.*

Concept	Magnitude	Consumption	Cost
Javier Krug	h	9.60	91.2
Benjamin	h	6	72
Aroa	h	5	75
Pedro Serna	h	1	20
Cristina	h	1	20
Precursor RuNONO2	g	0.1297	9.31
Purified water	ml	3	9.00E-06
Alumina	g	3	1.66
X-rays fluorescence	sample	6	189.84
TEM Microscopy	sample	1	77.11
X-Rays diffraction	sample	3	194.79
Hydrogen	ml	12000	0.20
Argon	ml	24000	1.30
Nitrogen	ml	24000	1.39
Internal Standard	ml	60000	1.34
Ammonia	ml	37440	2.95
Drying oven	kWh	6	0.97
Calcination oven	kWh	2	0.32
Reduction oven	kWh	2	0.32
Reactor oven	kWh	4.05	0.66
Chromatograph	ml He	9600	0.32
		Subtotal	760.68

***Table 6**.Cerium oxide catalytic test total cost.*

Concept	Magnitude	Consumption	Cost
Javier Krug	h	9.60	91.2
Benjamin	h	6	72
Aroa	h	5	75
Pedro Serna	h	1	20
Cristina	h	1	20
Precursor RuNONO2	g	0.1297	9.31
Purified water	ml	3	9.00E-06
Cerium oxide	g	3	2.01
X-rays fluorescence	sample	6	189.84
TEM Microscopy	sample	1	77.11
X-Rays diffraction	sample	3	194.79

Hydrogen	ml	12000	0.20
Argon	ml	24000	1.30
Nitrogen	ml	24000	1.39
Internal Standard	ml	60000	1.34
Ammonia	ml	37440	2.95
Drying oven	kWh	6	0.97
Calcination oven	kWh	2	0.32
Reduction oven	kWh	2	0.32
Reactor oven	kWh	4.05	0.66
Chromatograph	ml He	9600	0.32
		Subtotal	761.03

Table 7.*Hydrotalcite catalytic test total cost.*

Concept	Magnitude	Consumption	Cost
Javier Krug	h	9.60	91.2
Benjamin	h	6	72
Aroa	h	5	75
Pedro Serna	h	1	20
Cristina	h	1	20
Precursor RuNONO2	g	0.1297	9.31
Purified water	ml	3	9.00E-06
Hydrotalcite	g	3	0.35
X-rays fluorescence	sample	6	189.84
TEM Microscopy	sample	1	77.11
X-Rays diffraction	sample	3	194.79
Hydrogen	ml	12000	0.20
Argon	ml	24000	1.30
Nitrogen	ml	24000	1.39
Internal Standard	ml	60000	1.34
Ammonia	ml	37440	2.95
Drying oven	kWh	6	0.97
Calcination oven	kWh	2	0.32
Reduction oven	kWh	2	0.32
Reactor oven	kWh	4.05	0.66
Chromatograph	ml He	9600	0.32
		Subtotal	759.37

***Table 8**.Magnesium oxide catalytic test total cost.*

Concept	Magnitude	Consumption	Cost
Javier Krug	h	9.60	91.2
Benjamin	h	6	72
Aroa	h	5	75
Pedro Serna	h	1	20
Cristina	h	1	20
Precursor RuNONO2	g	0.1297	9.31
Purified water	ml	3	9.00E-06
Magnesium oxide	g	3	1.10
X-rays fluorescence	sample	6	189.84
TEM Microscopy	sample	1	77.11
X-Rays diffraction	sample	3	194.79
Hydrogen	ml	12000	0.20
Argon	ml	24000	1.30
Nitrogen	ml	24000	1.39
Internal Standard	ml	60000	1.34
Ammonia	ml	37440	2.95
Drying oven	kWh	6	0.97
Calcination oven	kWh	2	0.32
Reduction oven	kWh	2	0.32
Reactor oven	kWh	4.05	0.66
Chromatograph	ml He	9600	0.32
		Subtotal	760.13

***Table 9**.Silicium oxide catalytic test total cost*

Concept	Magnitude	Consumption	Cost
Javier Krug	h	9.60	91.2
Benjamin	h	6	72
Aroa	h	5	75
Pedro Serna	h	1	20
Cristina	h	1	20
Precursor RuNONO2	g	0.1297	9.31
Purified water	ml	3	9.00E-06
Silica oxide	g	3	6.69
X-rays fluorescence	sample	6	189.84
TEM Microscopy	sample	1	77.11
X-Rays diffraction	sample	3	194.79
Hydrogen	ml	12000	0.20
Argon	ml	24000	1.30
Nitrogen	ml	24000	1.39
Internal Standard	ml	60000	1.34
Ammonia	ml	37440	2.95
Drying oven	kWh	6	0.97

Calcination oven	kWh	2	0.32
Reduction oven	kWh	2	0.32
Reactor oven	kWh	4.05	0.66
Chromatograph	ml He	9600	0.32
		Subtotal	765.71

1.3 TOTAL COST OF THE RESEARCH

In this section the total cost of the research is appreciated in Table 10. Considering all the reactions carried out, the extra general cost calculated as 8% and the taxes which have been estimated as 21%.

Table 10. *Research total cost resume.*

Concept	Cost
Alumina reaction	920.43 €
Hydrotalcite reaction	918.45 €
Magnesium reaction	919.26 €
Cerium oxide reaction	919.61 €
Silicon oxide reaction	926.17 €
Subtotal	4,603.92 €
General Costs	368.31 €
Subtotal	4,972.23 €
Taxes	1,044.17 €
Total	6,016.40 €